FINAL REPORT
US Department of Energy

A HYDROLOGIC - GEOPHYSICAL METHOD FOR CHARACTERIZING FLOW AND TRANSPORT PROCESSES WITHIN THE VADOSE ZONE

David L. Alumbaugh
University of Wisconsin-Madison

Douglas LaBrecque
MultiPhase Technologies, LLC.

James Brainard
Sandia National Laboratories

T. C. (Jim) Yeh
University of Arizona

Project Number : 70267
Grant Number : DE-FG07-
Grant Project Officers: Dr. Roland Hirsch
Project Duration: 9/15/99-9/15/03

Table of Contents

1.0 Executive Summary

The primary purpose of this project was to employ two geophysical imaging techniques, electrical resistivity tomography and cross-borehole ground penetrating radar, to image a controlled infiltration of a saline tracer under unsaturated flow conditions. The geophysical techniques have been correlated to other more traditional hydrologic measurements including neutron moisture measurements and induction conductivity logs. Images that resulted during two successive infiltrations indicate the development of what appear to be preferential pathways through the finer grained materials, although the results could also be produced by cationic capture of free ions in clays. In addition the site as well as the developing solute plume exhibits electrical anisotropy which is likely related to flow properties. However the geologic significance of this phenomenon is still under investigation.

A secondary purpose was to alter existing geophysical imaging and hydrologic property estimation techniques to better account for spatial heterogeneity and other factors. For the electrical resistivity tomography this involved including electrical anisotropy in the algorithm, as well as accounting for the affect of subsurface temperature variations on electrical resistivity. For the hydrologic property estimation techniques, hydrologic tomography methods were developed and tested, problems associated with including moisture contents estimated from resistivity images thoroughly analyzed, and more robust methods for including geophysical data to condition the inversion incorporated.

The methods developed under this research are already impacting long term monitoring of enhanced environmental remediation of contaminants, with electrical resistivity tomography systems being implemented at several large-scale sites. In addition the other imaging and estimation techniques, as well as the infiltration testing method itself, have been now fully tested such that they are ready for deployment by the DOE as necessary.

The work involved a multidisciplinary team with specialization in geophysical image technologies, theoretical hydrology, and field scale experience. Two PhD dissertations and two MS theses resulted from the project (see section 7.0 for list) which can be obtained by contacting the departments at the respective institutions.

2.0 Research Objectives

Many DOE facilities inadvertently have released toxic or radioactive wastes into the unsaturated, or vadose zone, that comprises the near-subsurface beneath their sites. Contamination sources include leaky underground storage tanks and landfills, as well as cribs, ponds and trenches where hazardous wastes were essentially dumped on the ground and allowed to infiltrate (GAO, 1998). Such waste disposal methods were the result of not fully appreciating the potential public health hazards posed by the contaminants, as well as a lack of awareness of the complexity of vadose zone flow and transport processes. This complexity and our continued lack of ability to account for important flow and transport processes in predictive modeling is underscored by the many documented cases of contaminants being found where they are not expected and/or not predicted. For example, at Yucca Mountain in Nevada, chlorine 36 from airborne nuclear detonations at the Nevada Test Site during the 1950's was found at much greater depths than thought possible.

Inaccurate estimates of vadose zone flow and contaminant transport rates most likely result from simplifying assumptions required by the large scale and complexity of real world problems as well as the inability to incorporate pertinent physics governing flow and transport within the vadose zone into predictive models. These assumptions range from the treatment of heterogeneity where clastic sedimentary formations typically have complex hierarchical assemblages of bedforms. Here the structure and hierarchy of the bedforms are the end result of complex geologic and hydrologic processes. For example differences in sediment supply and stream flow can produce lateral and vertical variations in the bedforms at a variety of scales. It is very difficult to measure of the spatial variability of these systems due to the large number of samples required to statistically describe the full nature of the heterogeneity. Air permeameter techniques show promising results in rectifying this problem (cf. Davis et al, 1994), but such measurements require extensively exposed outcrops. An obvious example of the need to adequately account for heterogeneities in the vadose zone is underscored by the common observation of preferential flow where small perturbations tend to grow with time eventually producing finger like flow paths producing fast transport pathways.

A second problem associated with characterizing/modeling heterogeneous deposits is measuring hydraulic properties and up-scaling these properties to formation scale. Often field samples are collected from borehole cores or from excavations at a site. Hydraulic properties are then determined through laboratory procedures where significant precision and accuracy errors are commonly introduced. This error arises not only from the experimental method, but also from using repacked samples where little, if any of the original pore structure remains intact. The measurement error from hand samples may greatly exceed the spatial variability present in geologic formations.

Additional problems in predicting flow and transport within the vadose zone is 'heterogeneity' resulting from direct human intrusion. For example, a report released by DOE on the Hanford site (DOE,1998) has identified man made structures such as unsealed wells penetrating contaminated zones, and funnel flow around tanks and waste cribs, as possible mechanisms for increased rates of contaminant migration. How these man made structures couple with the naturally occurring hydrologic conditions to influence transport is not well understood. Because of this, the estimated rates of contaminant migration within the vadose zone may often be in error.

A better understanding of flow and transport modes within the vadose zone beneath DOE sites, including the influence of heterogeneity and man made structures, could lead to better conceptual models and therefore to better estimates of contaminant transport properties and rates. Incorporating this knowledge into predictive and performance assessment models would provide a sound basis for characterizing and/or removing some of the unknowns plaguing these programs. To address some of these issues, we performed a series of intermediate-scale field experiments to test assumptions concerning flow and transport mechanisms within vadose zone materials comprised of clastic sedimentary deposits similar to those underlying Hanford and other DOE sites in the western United States. The experiments involved geophysical imaging of water followed by a solute tracer introduced under controlled conditions at the ground surface. In addition we developed a series of numerical geophysical/hydrologic property estimation tools that allow for better estimates of spatial heterogeneity of hydrologic properties within the vadose zone. The benefits of the work to the DOE include:

- Better conceptual models regarding flow and transport mechanisms active in natural heterogeneous vadose zone deposits and such deposits altered by human intrusion.

- A database that predictive and performance assessment models describing flow and transport in the vadose zone could be compared to.
- A method to provide a check on current state of the art hydrologic modeling schemes to determine their applicability to real world problems.
- Validated experimental and numerical methods that could be applied to other DOE sites to determine site-specific flow and transport rates.

3.0 Methods and Results

3.1 Background

The research performed under this project had two related, yet separate objectives. The first was to perform a field-scale unsaturated flow/transport experiment, whereby two geophysical imaging technologies, electrical resistivity tomography (ERT), and cross-borehole ground penetrating radar imaging (XBGPR), along with other hydrologic and geophysical sensors, were employed to monitor changes in electrical conductivity caused by the addition of solute (in this case sodium chloride) to a steady-state infiltration process. Sodium chloride causes changes in electrical conductivity due to an enhancement in the number of charge carrying ions. Thus, imaging changes in electrical conductivity during solute infiltration allows us to track the spatial changes in tracer location as it moves through the system, and therefore investigate transport processes *in-situ*.

A secondary objective of our research was to develop cost-effective algorithms for identifying distributions of heterogeneity and contaminants within the vadose zone, and to improve upon existing geophysical imaging algorithms. Success of this project would eliminate the need for extensive and costly destructive sampling of media and maximize the information obtained from limited field sampling campaigns. Importantly, it would allow rapid and economic identification of spatial distributions of heterogeneity and contaminants in vadose zones so effective remediation operations could be designed and the progress of such efforts to be monitored in a more efficient manner.

3.2 Geophysical Imaging and Estimation Techniques

As described above, different geophysical measurement technologies were employed during the field experiment to detect and image changes in the subsurface caused by the flow/transport processes that were occurring. For completeness a brief description of the methods are provided here.

3.2.1 The electrical resistivity tomography (ERT) method

The ERT method involves the measurement of electric potential-differences between a series of electrodes that are generated by a current that is injected into the subsurface. Typically this involves the emplacement of multiple vertical electrode strings (VES) in the ground where the electrodes are equally spaced from the surface to depth. Additional electrodes can also be placed just beneath the surface. Images of the electrical conductivity structure are provided via numerical inversion of the voltage measurements.

During data acquisition, each electrode pair may serve both as a source as well as a receiver multiple times. Tens-of-thousands of unique data points may be collected during a three-dimensional survey such as that conducted at the Socorro site, and data may need to be collected multiple times in order to image transient subsurface processes. This obviates the need of automated systems for fast, efficient acquisition. In addition, the large amounts of data necessitate the use of optimized inversion algorithms that incorporate apriori geological knowledge to produce accurate 3D images of electrical conductivity. The schemes developed and used here are outlined in section 5.3 as well as in Appendix A.

3.2.2 The cross-borehole ground penetrating radar (XBGPR) method

Cross-borehole ground penetrating radar makes use of the fact that an electromagnetic wave propagates with different velocities through materials of different dielectric constant. Because the dielectric constant of unsaturated porous materials is largely dependent on the volumetric water content, the spatial variation in EM wave velocity can be directly related to variations in moisture content. More importantly for this experiment, EM waves exponentially attenuate in electrically conductive media, with greater rates of attenuation attributed to higher conductivity. Thus by imaging changes in attenuation over time, one can track the progress of a solute plume. More details on GPR theory can be found in Appendix B.

The XBGPR system uses a borehole antenna which transmits a high-frequency electromagnetic pulse outward in all directions. The center frequency of the system used at the Socorro site was 100 MHz.

The pulse is sensed by a receiver antenna located in a second borehole some distance away. The time varying voltage-waveform measured at each receiver location is then processed to extract the EM wave travel time from the source to the receiver, and the transmitter-normalized amplitude (see Appendix B for more details). These data are then inverted to produce 2-D images of velocity and attenuation, respectively. The velocity image is converted to moisture content using a site-dependent conversion (Alumbaugh, et al., 2002).

3.2.3 Borehole geophysical logging methods

Two other types of borehole measurements were collected during the infiltration experiment; neutron moisture and electrical conductivity logs. Neutron moisture measurements employ back-scattered neutrons to detect the presence of hydrogen nuclei. Because the number of neutrons that are back-scattered is proportional to the amount of hydrogen that is present, increasing water contents will cause higher rates of detected neutrons at the receiver. Through a site specific calibration process this can lead to accurate estimates of moisture content as a function of depth along a borehole.

Electromagnetic conductivity logs use electromagnetic induction of currents within a medium to estimate electrical conductivity along a borehole. The greater the electrical conductivity of the formation, the larger the induced currents generated in the medium, and hence the larger the scattered magnetic field measured by the receiver. A Geonics EM-39 was employed in the experiment described below.

3.3 Theoretical Developments

To augment the experiment and provide for better, more realistic interpretations of the geophysical field data, theoretical modifications were required for the electrical resistivity inversion codes. In addition research continued on the hydrololgic property estimation techniques originally developed under EMSP Project # 55332. Both of these subprojects led to better methods for incorporating realistic heterogeneity into subsurface property estimations.

3.3.1Theoretical Developments in Electrical Resistivity Tomography Imaging

The resistivity of sediments is primarily dependent on porosity, pore-water saturation and conductivity, and the presence of clays with high cation exchange capacities, and is only weakly dependent on factors such as grain size and texture (Archie, 1942, Brace, 1977). In unsaturated sediments within the vadose zone, the water content depends on the retention capacity of the soil that in turn varies dramatically with grain size. Thus, a layered sediment sequence that appears electrically homogeneous and isotropic under saturated conditions may be highly inhomogeneous and/or anisotropic when only partially saturated. Although the importance of anisotropic effects has been known almost since the inception of resistivity surveys (Kunz and Moran, 1958), due to the complexity of including anisotropy within the interpretation, these effects are almost always ignored in electrical resistivity tomography as well as traditional resistivity surveys on the surface.

Generally, the distribution of the electrical potential in the earth is governed by the continuity equation,

$$\nabla \bullet \hat{\sigma} \nabla \mathrm{V} = \mathrm{I} \ , \qquad (1)$$

where V is the scalar electrical potential and I is the distribution of electric current sources in the media. The electrical conductivity at a point in the earth can be represented by a full symmetric tensor of the form:

$$\hat{\sigma} = \begin{bmatrix} \sigma_{x,x} & \sigma_{x,y} & \sigma_{x,z} \\ \sigma_{x,y} & \sigma_{y,y} & \sigma_{y,z} \\ \sigma_{x,z} & \sigma_{y,z} & \sigma_{z,z} \end{bmatrix} . \qquad (2)$$

where $\hat{\sigma}$ is the tensor conductivity; $\sigma_{x,x}$, $\sigma_{y,y}$ and $\sigma_{z,z}$ are the conductivities in Cartesian coordinate directions and $\sigma_{x,y}$, $\sigma_{x,z}$, and $\sigma_{y,z}$ are cross-terms. Six independent parameters are needed to fully

describe the conductivity tensor which can be thought of as an elliptical volume. If the axes of this conductivity ellipsoid are aligned with the coordinate directions, then cross-terms go to zero and Equation (2) simplifies to

$$\hat{\sigma} = \begin{bmatrix} \sigma_{x,x} & 0 & 0 \\ 0 & \sigma_{y,y} & 0 \\ 0 & 0 & \sigma_{z,z} \end{bmatrix} . \qquad (3)$$

For the special, though common, case of horizontally layered and anisotropic media where $\sigma_{x,x} = \sigma_{y,y}$, the coefficient of anisotropy , λ, is defined as (Keller and Frischknecht, 1966)

$$\lambda = \sqrt{\sigma_{x,x} / \sigma_{z,z}} \quad . \qquad (4)$$

For this case, it can be shown that resistivity measurements made using only electrodes oriented in a vertical line (as in traditional resistivity well logging), are sensitive only to the horizontal resistivity and measurements made on a horizontal plane, (as in traditional surface resistivity measurements) measure the geometric mean of the horizontal and vertical resistivities (Kunz and Moran, 1958, Keller and Frischknecht, 1966). Thus, using either borehole or surface resistivity measurements alone produces consistent though somewhat erroneous results. However ERT measurements include a full range of acquisition geometries including both vertical to horizontal arrays, as well as various other combinations. This creates an incongruity between the measurements such that for a layered anisotropic earth there is no coarsely layered isotropic model that will closely match all of the measurements. To alleviate this problem, a 3-D anisotropic inversion algorithm using an Occam's inversion approach was developed as described in Appendix A.

Temperature corrections are commonly included in well logging applications where the exploration depth is great enough to be affected by the geothermal gradient (Hearst and Nelson, 1985). Temperature corrections have also been used for very shallow agricultural applications of electromagnetic methods such as predicting moisture content (Sheets and Hendrickx, 1995) and root-zone salinity (Slavich and Petterson, 1990). In this case, temperature corrections were deemed necessary since annual temperature variations in the upper few meters of soil were large enough to affect conductivity measurements.

Fluid resistivity (the inverse of conductivity) is proportional to fluid viscosity, which in turn inversely proportional to temperature. Arps used empirical data from sodium chloride solutions to obtain an equation that is commonly used in well logging applications where the exploration depth is great enough to be affected by the geothermal gradient (Nelson and Hearst, 1985). Expressing Arps' Equation in terms of electrical conductivity and temperature in Centigrade yields the equation,

$$EC_2 = EC_1 \frac{T_2 + 21.5}{T_1 + 21.5} , \qquad (11)$$

where EC_1 is the fluid conductivity at temperature T_1 and EC_2 is the fluid electrical conductivity at temperature T_2.

At the experimental site described below, the imaged resistivities were corrected to 25° C to be consistent with fluid sample data. To apply the correction, subsurface temperatures were determined by 3-D Kriging of thermocouple data, the locations of which are described below and in Brainard et al (2003). The Kriged temperatures were then used to perform a pixel by pixel correction for the electrical conductivity images determined by ERT.

An example showing the effects of this correction at the Socorro site is given in Figure 1. Here both images of temperature corrected and uncorrected electrical conductivity are shown for data collected in July 2002 after a saline injection test had ended. At the Earth's surface, the peak-annual temperatures in

Socorro occur in mid July. Without corrections, the image to the left shows a number of shallow anomalies that could be misinterpreted as lateral movement of the saline tracer injected on the site. The temperature corrected image to the right gives a much clearer picture of the extent of the tracer.

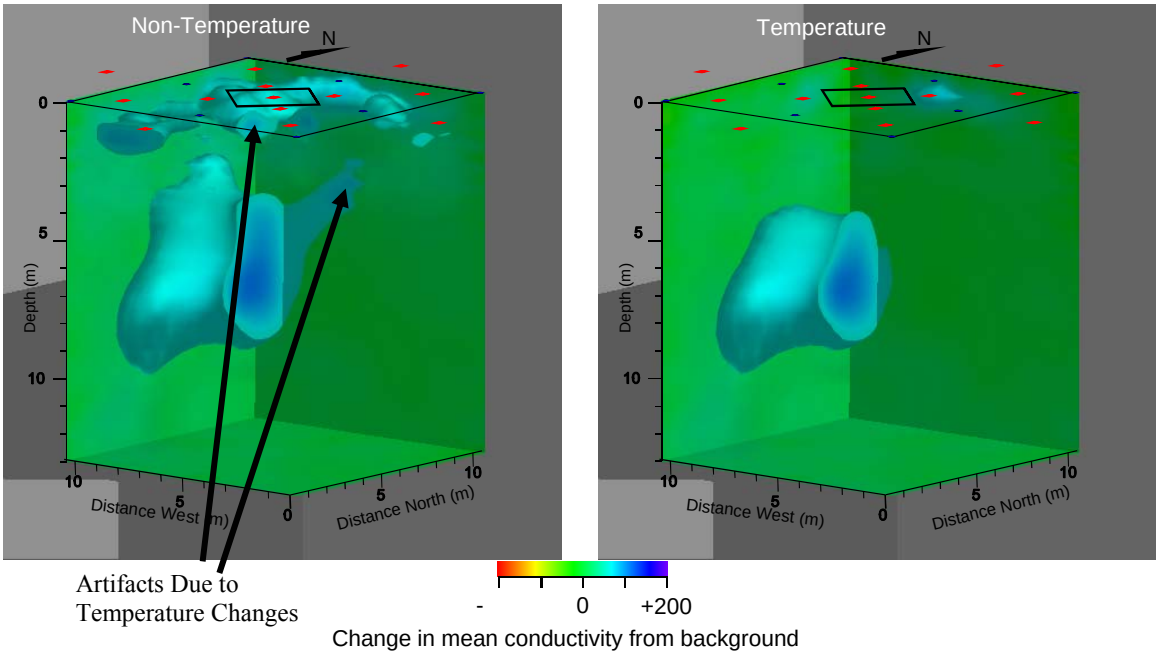

Figure 1 – Images of electrical conductivity difference from ERT data collected during the Socorro infiltration experiment (left) without the temperature correction, and (right) with the correction.

3.3.2 Theoretical Developments in Hydrologic Property Estimation

Theoretical advances were also made in the broad area of estimating subsurface hydrologic properties using sparse hydrologic and remote geophysical measurements. These algorithms incorporate information about moisture content and pressure distributions to delineate heterogeneity in the vadose zone, and employ arrival times of wetting or drying fronts at depth to determine hysteretic characteristics of unsaturated hydraulic properties from field studies. We also continued our work in analyzing the spatial correlation between electrical resistivity and moisture content within the vadose zone. The hope was that a better understanding of the nature of the correlation including the uncertainty would allow us to better us electrical resistivity ERT surveys to provide more reasonable geological / hydrologic interpretations.

The previous EMSP project (EMSP Project # 55332) saw the initial development of an iterative stochastic approach to estimate conditional effective unsaturated hydraulic parameters using soil-water pressure head, degree of saturation, and concentration during transient flow and transport processes in heterogeneous vadose zones. The successive linear estimator (SLE) ((Hughson and Yeh, 2000; Vargas-Guzman and Yeh, 2002) that employs covariances of unsaturated hydraulic parameters, soil-water pressure head, degree of saturation, and concentration, as well as the cross-variances of these parameters, is central to this iterative approach. Successive improvement in the linear estimator is achieved by solving the governing flow and transport equations, and updating the residual covariances and cross-covariance functions in an iterative manner. Using this iterative approach, the nonlinear relationships between unsaturated hydraulic conductivity parameters, degree of saturation, head, and concentration can be incorporated in the estimation. Consequently, more detailed spatial distributions can be obtained than available from field observations or specified data in computational studies using this technique.

Detailed computational studies with this model (Hughson and Yeh, 2000) indicated that pressure and moisture content data sets from fixed locations collected at later times during an infiltration event, or during steady state flow, provided better estimates of the hydrological parameters of the vadose zone than data from very early times. In addition, these studies indicated that sequentially conditioning on multiple sets of pressure data obtained at different times would yield better results than conditioning using only a

single time. As important, the computational studies indicated that artifacts could be produced that were dependent on nature of the spatial density (or sparseness) of the data, and how well the associated boundary conditions are known. This finding suggested that complete characterization of heterogeneity requires extensive sets of pressure and moisture content data covering the entire physical domain considered for our inverse model, which in a field sense is grossly impractical.

Additional questions regarding the utility of our inverse methodology and data requirements were addressed in the new project through further computational studies (Yeh and Liu, 2000) and sandbox experiments under well-controlled laboratory conditions (Liu, Yeh, and Gardiner, 2002). Simulations of pumping tests in two-dimensional, heterogeneous aquifers were used to investigate optimal sampling schemes in terms of selection of well spacing, pumping, and monitoring locations. The effects of measurement errors and uncertainties in statistical parameters required for the inverse model were also included in these investigations. Results of these numerical experiments showed that hydraulic tomography would be most effective if the horizontal distance between wells half the value of the horizontal correlation scale. In addition, the vertical interval between two monitoring locations should be no more than half of the vertical correlation scale. Of particular importance for practical applications, the optimal number of pumping locations is determined by the ratio of the thickness of the section under consideration to the vertical correlation scale. An increase in the number of pumping locations above this ratio provides no additional information.

These numerical experiments also led to the conclusion that uncertainty in the input variance and correlation scales had no influence on the final estimate, unless the correlation scales were unrealistically underestimated or overestimated. In addition, increasing secondary information, such as pressure head data, at different spatial locations can greatly reduce the effects caused by a poor knowledge of the correlation structure. Similar conclusions were supported by extension of the numerical experiments to a three-dimensional, heterogeneous aquifer.

Sandbox experiments were used to validate the conclusions arising from the numerical experiments and to evaluate the performance of our inverse methodology under physically realistic conditions. One sandbox was packed with layered sands to represent a stratified aquifer and the second was packed to yield discontinuous bodies of different shapes and dimensions to represent a more complex heterogeneous aquifer. For both sandbox experiments the inverse model was able to reproduce the major heterogeneous patterns, in spite of measurement errors and uncertainties associated with the pressure head/discharge data and other required input parameters. One significant outcome from these experiments was that hydraulic tomography does not improve the conductivity estimate if an abundant number of head measurements is available, particularly in the case of stratified media. However, hydraulic tomography is useful when the number of pressure head measurements is limited or for those cases of heterogeneous aquifers that possess a highly discontinuous and nonuniform structure. The sandbox studies also demonstrated the utility of inverse modeling in designing hydraulic data sampling strategies.

These studies also verified the earlier conclusions that the amount of hydraulic data required to achieve accurate estimates make field-scale implementation of the approach unreasonable. As a consequence, we continued to explore the possibility of incorporating geophysical measurements closely tied to moisture content, such as ERT, to provide the secondary data required for our inverse model (Yeh and Simunek, 2002). The resulting stochastic fusion approach iteratively couples unsaturated hydraulic tomography and ERT data to yield a more detailed image of hydraulic heterogeneity. To implement this at the field scale, an unsaturated hydraulic tomography experiment is conducted by sequentially using several different water infiltration locations. Limited point measurements of pressure head and moisture content are collected in conjunction time-lapse ERT data. The inversion then proceeds as a three-step process. 1) The mean hydraulic parameters from the unsaturated hydraulic tomography are used in a forward simulation to yield the mean and covariance structure of the resistivity and moisture content fields. 2) This information is employed within the ERT inversion to estimate changes in resistivity and moisture content, as well as the moisture content and conditional moments. 3) The updated resistivity and moisture content fields serve as new input to the hydraulic tomography inversion model to yield improved estimates of the unsaturated hydraulic parameters and their conditional moments. This process continues in an iterative manner until no further improvement in hydraulic heterogeneity, moisture content, and resistivity estimates is gained.

The advantages of this new approach are that information regarding moisture content at locations where no samples are available is provided by the ERT, while the sampling data from the hydraulic tomography test provides additional constraints for inversion of the ERT data. However, applications of

ERT to field experiments have led to a new finding and complications. Translating estimated resistivity fields to moisture content fields has to rely on calibration (i.e., the Archie's law) and curves derived from field samples have shown that the relation between resistivity and moisture content varies significantly in space. As a result, the image of resistivity change may not reflect true changes in the moisture content during infiltration (Yeh et al., 2002) which can lead to unreasonable estimates of hydraulic properties. To overcome this complication, we have developed a new approach to estimate moisture content directly that uses resistivity/moisture relations obtained directly from core samples to condition the ERT inversion. This approach can also include measurements of neutron probes such that a more direct estimation of moisture content in space is possible (Liu and Yeh, 2004).

3.4 Field Results

3.4.1 Site Description

The experiment was conducted the Sandia/Tech Vadose (STVZ) facility (Figure 2). The STVZ was constructed for an earlier EMSP project (see Project # 55332) and a report by Brainard et al., (2003) provides a detailed description of site geology, hydrologic characterization, instrumentation, infiltration system, and data acquisition methods as well as results from the previous project. As such, most of the information provided by Brainard et al (2003) on instrumentation, infiltration, and data acquisition are pertinent to this project. A brief description of the modifications and the experimental site is given below and a more complete description can be found in Brainard et al (2004).

The STVZ facility is located adjacent to the New Mexico Institute of Mining and Technology campus in Socorro, NM on poorly consolidated, heterogeneous alluvial deposits comprised of inter-bedded sands, gravels, and clays exhibiting heterogeneity on scales ranging from micro-structures through small scale cross-bedding to fairly homogenous beds as thick as 7 meters. Cuttings from 41 instrumentation boreholes and 4 continuous core samples located axi-symmetrically about the center of the infiltrometer (Figure 3) and drilled to depths up to 12 m provided the data for developing a stratigraphic model of the deposits. Electromagnetic induction and natural gamma borehole logs from all 41 holes aided in locating and verifying contacts between units of contrasting electrical conductivity, while two trenches excavated to 1.5 m on the hill slope adjacent to the instrument pad and exposures in a nearby sandpit provided additional geologic information on the character of the deposits. Four simplified stratigraphic columns are depicted in Figure 4, along with a likely correlation between mappable geologic units.

The site is instrumented with arrays of transducer- equipped tensiometers, suction lysimeters, TDR probes, thermocouples, and electrode arrays for collecting Electrical Resistivity Tomography (ERT) data; a plan-view of instrument locations along with identifiers is given in Figure 3. Thirteen PVC pipes measuring 2 inches in diameter provide access for down-hole geophysical measurements including XBGPR and electromagnetic induction logs. All arrays are arranged axi-symmetrically about the center on the 3-m square infiltrometer. The instrument arrays interrogate a volume approaching that of actual contamination plumes (approximately 3000 cubic meters).

The eight vertical electrode arrays each consist of 17 electrodes that are evenly spaced from the surface to 12m depth. An additional 36 electrodes are installed across the surface. Using a pole-pole type array configuration results in approximately 10000 possible data combinations. Five PVC cased boreholes along a transect extending from the southwest to the northeast section of the site as shown in Figure 3 were employed in collecting the XBGPR data. The down-hole sampling interval employed was 0.25m with a center frequency of 100 MHz. This resulted in four cross-borehole planes of data that were simultaneously inverted to produce the 2D images on each date.

The infiltrometer was designed to provide an even flux of potable water and tracer solution over a 3 by 3 meter infiltration surface. Implementing the tracer experiment required adding components to the original infiltrometer water supply system (see Brainard et al. 2003 for a description of the original water supply system). However, the original infiltrometer itself was not modified for the new set of experiments, and consists of 9 separate infiltration panels each consisting of 100 evenly spaced stainless-steel medical needles. The surface boundary condition also incorporates an impermeable buried polyurethane tarp extending beyond the surface area above the instrumentation to prevent gains and loses in subsurface water contents arising from precipitation and evaporation.

The original water distribution system incorporated two 500-gallon potable water supply tanks connected to a common infiltrometer supply line. The addition of a third 500-gallon tracer solution supply tank, pump, flow control, flow monitoring equipment and infiltrometer supply line provided the ability to infiltrate the tracer solution independently of the potable water. The water and tracer solution was pressurized with separate pumps and stored in separate diaphragm pressure tanks. Infiltration was initiated for five minutes twice daily using a timer and heavy-duty solenoids in both lines. During the infiltration events, the potable water and the tracer solution were independently fed to the routing station where the water and tracer solution could be exclusively routed to any of the nine infiltration panels. Flow to each of the nine infiltration panels was controlled by a pressure regulator and monitored with a flow meter. This setup allowed for independent monitoring of, and adjusting the flow to, each of the nine panels to assure an even flux across the infiltration surface. See Brainard et al. (2003) for a detailed description of the infiltration system.

Figure 2: View of the site looking to the northwest. The infiltrometer covered by the white PVC tarp just to the left of center in the photograph. Surrounding the infiltrometer in an axi-symmetric pattern are 13 PVC access tubes (smaller diameter pipes) and covers for the tensiometer access tubes (larger diameter pipes). The building houses all of the data acquisition equipment and water/tracer supply tanks and equipment. The center access tube discussed later in this report is located at the center of the infiltrometer and is covered by the tarp.

3.4.2 Pre-Solute Infiltration Geophysical Images

Figures 5a and 5b show 3-D images of the anisotropic electrical conductivity of the site as estimated from the ERT images prior to the transport experiments, while Figure 6 shows the 2-D moisture content and attenuation images derived from the GPR data along the SW-NE profile. In the ERT images, regions of conductive, fine-grained, clay and silt bearing layers with relatively high water content appear as dark blue, while dry-resistive zones are shown as shades of red; the opposite color scale has inadvertently been used for the GPR images in Figure 6. Although the water saturation below the infiltrometer increases the conductivity by roughly a factor of two in this region, it is difficult to see in these "absolute images" since the range in background resistivity values is very large. In the GPR images the increased moisture content is somewhat easier to see as regions of increased moisture content and attenuation extending upward to the surface in the center of the image. These images highlight the general geology of the site as consisting of interbedded clays (conductive), sands(intermediate) and gravels (resistive), and serve as the

background images for the differences that are computed to highlight the changes caused by the solute infiltration.

Further analysis of Figures 5a and 5b, the horizontal and vertical conductivity, indicate the magnitude of resistivity anisotropy at the site. Most of the site (approximately 62%) has values of λ (the coefficient of anisotropy in equation A4) between 1.25 and 1.75. Thus horizontal conductivity is 1.5 to 3 times higher than the vertical conductivity. Although λ tends to be higher within the known clay/silt bearing layers, there is not a simple, clear-cut relation between the known geology, the hydrology, and λ. Furthermore, at least some of the anomalies appear to correlate with the electrodes. For example, at the bottom, center of Figure 5b, there are series of small anomalies reminiscent of beads along a vertical string.

A closer analysis of Figure 6 also shows an interesting relationship between the GPR derived moisture content and attenuation. First, the regions of high-attenuation tend to extend more continuously across the section than do corresponding regions of high moisture content. Because core records indicate that these areas of high moisture content/attenuation correspond to clay zones, it appears that the attenuation images are better at mapping zones of higher clay content. In addition the figures show that the maximum in moisture content often lies just above the maximum in attenuation. This was suggested by Chang et al (2003) to possibly be indicative of regions of higher moisture content 'perched' on top of impermeable clay zone. However, initial simulations performed under a new EMSP project indicate that this may be an artifact of the imaging process.

3.4.3 The Transport Infiltration Experiment

3.4.3.1 Experimental Design

Two constant flux tracer experiments followed an extended constant flux experiment (815 days) where potable water was infiltrated at an average flux of 2.97 cm/day (Standard deviation of 0.18) across the 3 by 3 meter infiltration surface. During this extended period of potable water infiltration, a steady state flow field was developed providing the ability to attribute changes in resistivity and the dielectric properties of the medium to the presence of the NaCl tracer rather than to influences due to changing moisture contents. Images of the steady-state moisture field are given in Figure 7.

During the first tracer experiment, a low conductivity NaCl solution (275 mS/m) was supplied to three of the nine infiltration panels (Figure 3). After this initial tracer experiment, potable water (80 mS/m) was once again infiltrated across the entire infiltrometer to flush the tracer from the first experiment away from the measurement field; this lasted 53 days. A second higher concentration solution (1,300 mS/m) was infiltrated through 3 of the nine panels (Figure 3) for 85 days. Once again potable water was routed to all nine of the panels for an additional 57 days at which time infiltration at the site ceased. Various measurements continued at the site for an additional 21 days beyond the end of infiltration.

In addition to the ERT and XBGPR data, subsurface monitoring and data collection included subsurface temperatures with thermocouples installed at 2, 4, 6,and 8 meter depths at two locations in each quadrant, moisture content with a CPN neutron moisture meter, electromagnetic conductivity with a Geonics EM-39 induction logging tool, and fluid conductivity data from solution samplers. In addition to subsurface monitoring, infiltration rates and tracer solution conductivities were also monitored. The infiltration rates were monitored both with pressure transducers installed in the bottom of the water tanks and by manual measurements of water depth as seen through the translucent supply tanks.

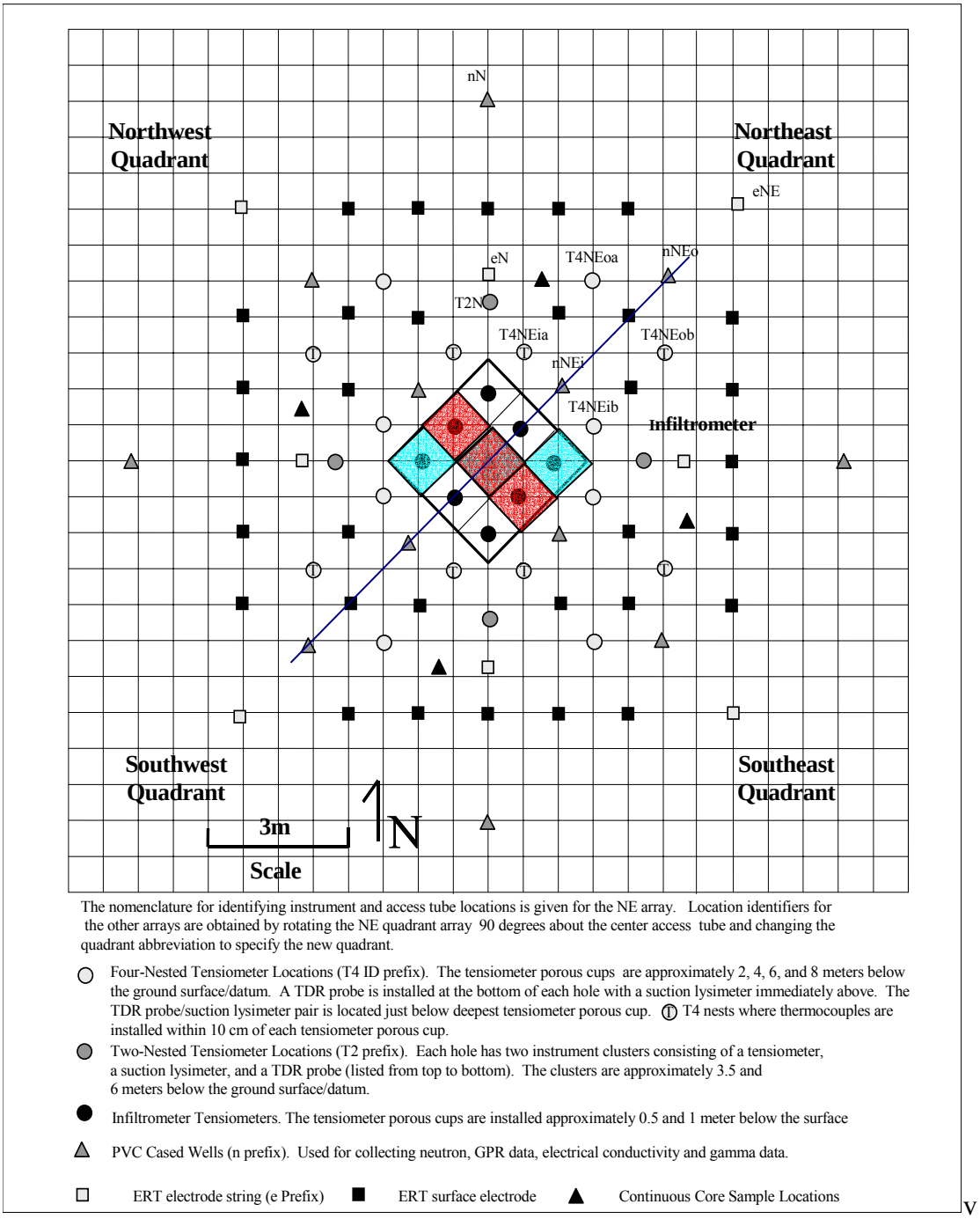

Figure 3: Plan-view schematic of the instrument pad giving the nomenclature and location for the various sensors. The three infiltrometer arrays through which the tracer was infiltrated during the first experiment are shaded blue, and the second those used during the second experiment are red. The blue line extending diagonally across the site designates the XBGPR profile location.

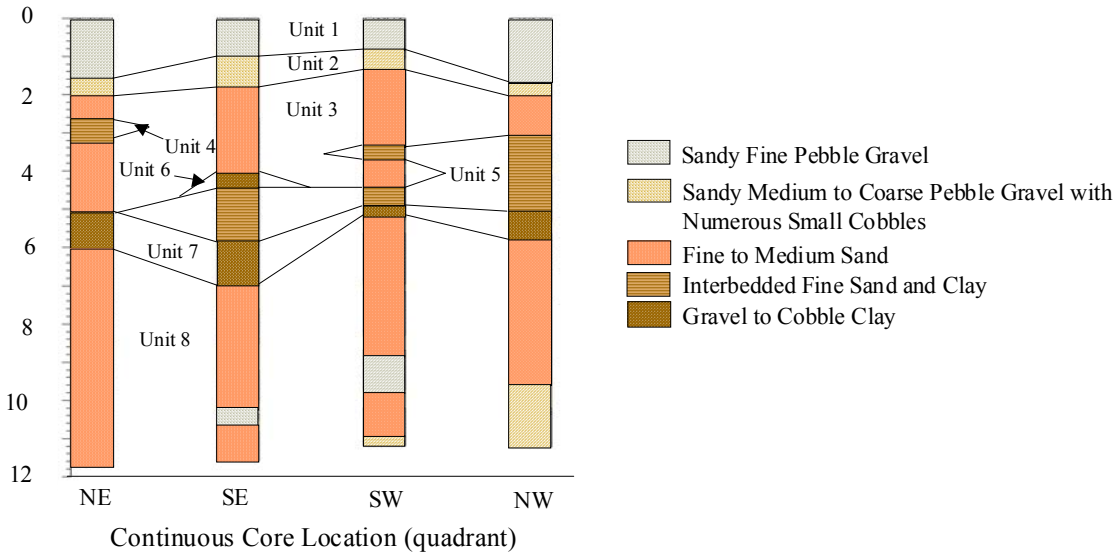

Figure 4: Generalized stratigraphic columns depicting geologic units and possible stratigraphic correlations. The geologic data was obtained from four continuous core samples collected from the locations indicated in Figure 2.

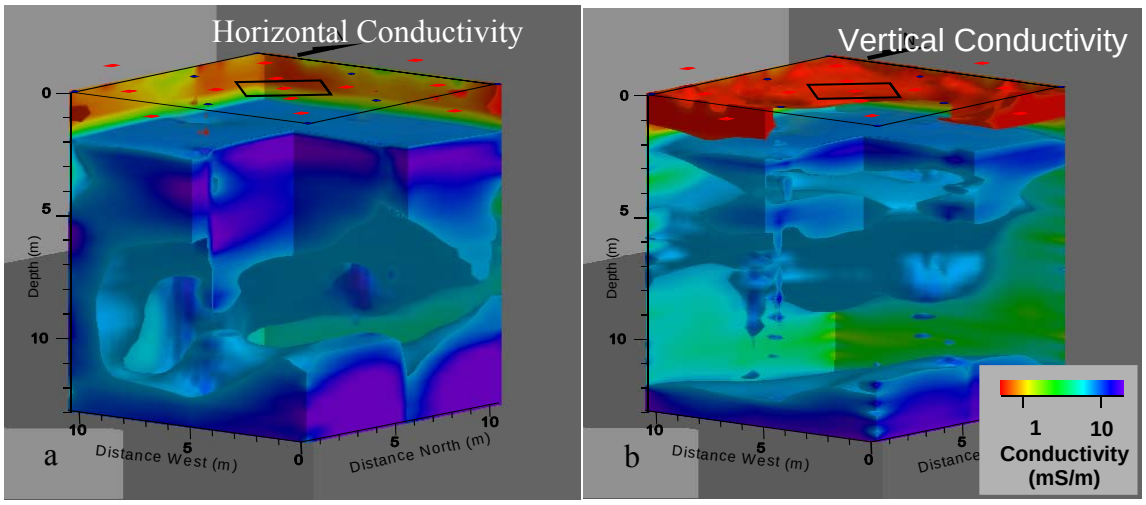

Figure 5: Images of horizontal (a) and vertical (b) conductivity at the Sandia Tech. Vadose Zone site prior to the beginning of the transport experiment. The images were derived from three-dimensional anisotropic inversion of ERT data.

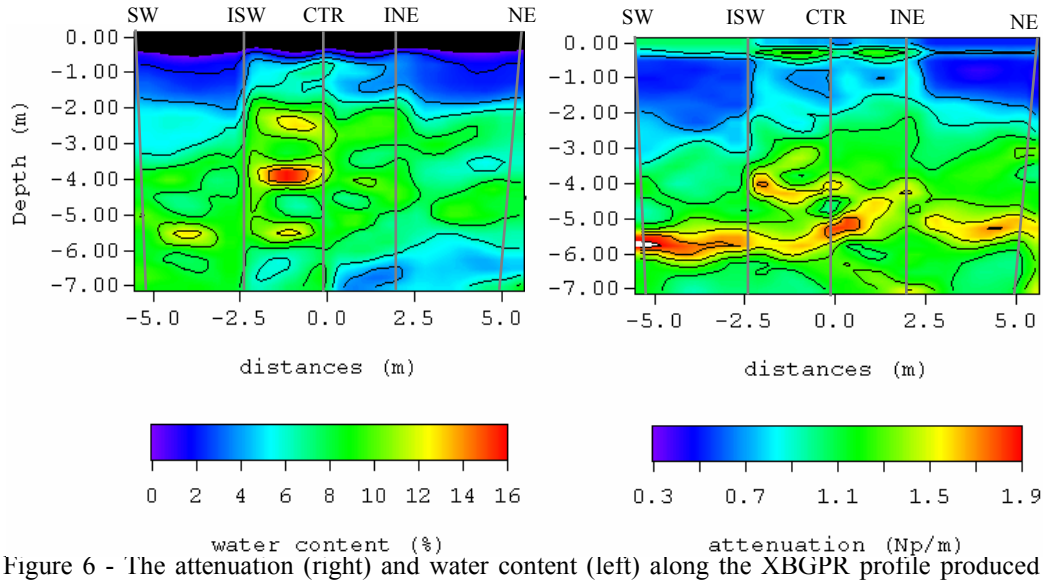

Figure 6 - The attenuation (right) and water content (left) along the XBGPR profile produced from data collected 4 days before the second salt infiltration initiated. Locations of boreholes are also shown on the images.

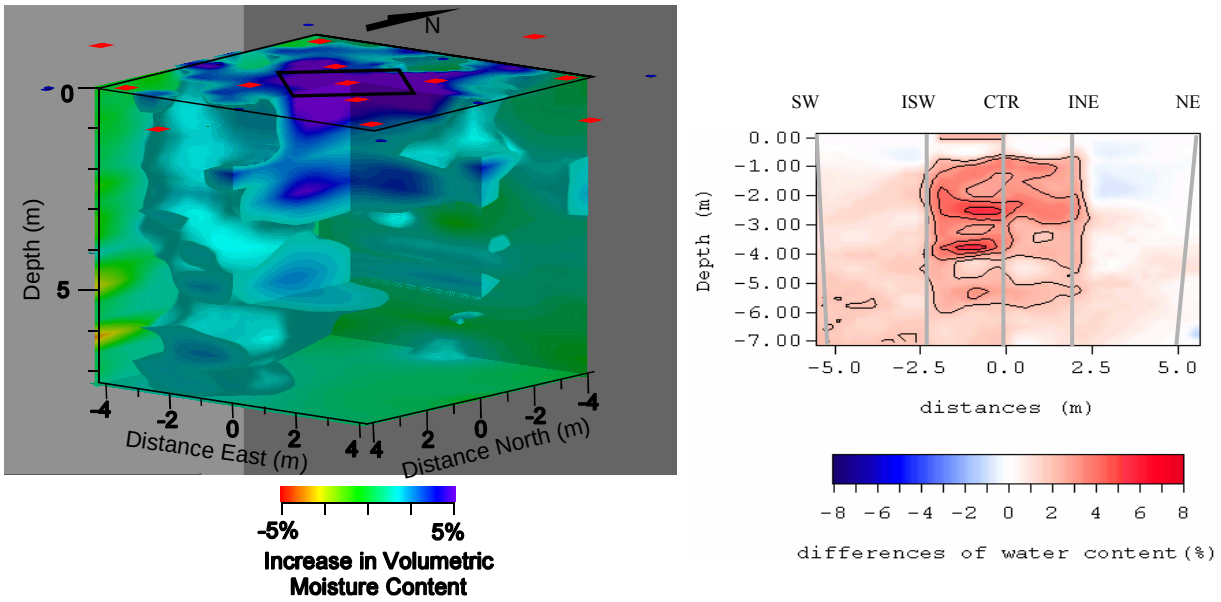

Figure 7 – The steady-state moisture content field imaged using the ERT data (left) and XBGPR data (right). Note that the color scales are reversed in the two different images.

3.4.3.2 Results

Brainard (2003) has shown that obtaining flow rates from the tanks using pressure transducers compared very well to flow data obtained from manually recording water levels and flow meter data. In this report only flow data from pressure transducers will be presented. Plots of the potable water, tracer solution, and total flux in for the period covering 100 days before the first tracer experiment (experimental day 700) through the second tracer experiment to the end of infiltration (experimental day 1237) are given in Figure 8 while the average and standard deviation of the flux for each phase of the experiment is given in Table 1. The plots show that infiltration rates were not extremely consistent in the short term as indicated by irregular upward and downward spikes in the data. These spikes probably result from adjustments made at the routing station where flow to each of the nine panels was adjusted to obtain an even flux across the infiltration surface. The long-term flow of both the tracer and the potable water was, however, fairly consistent throughout the series of infiltration/tracer experiments and remained in the range 2.94 and 3.01 cm/day (Table 1)

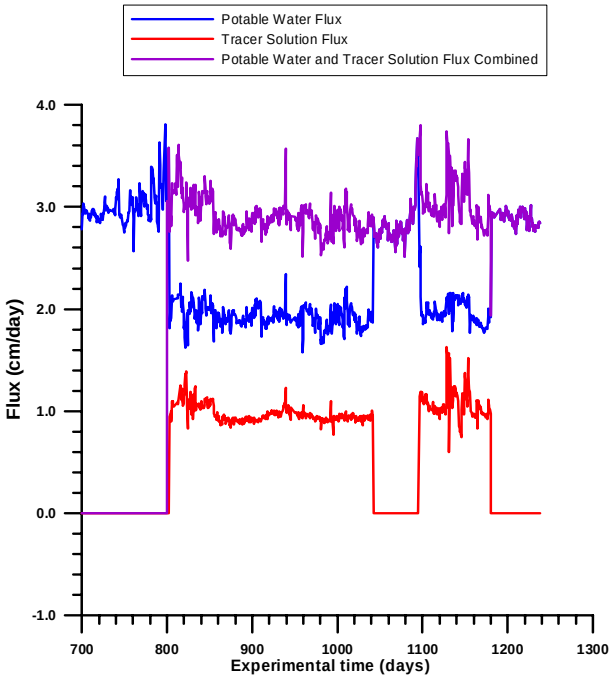

Figure 8: Plot showing the potable water, tracer solution, and total flux at the infiltrometer. Potable water was infiltrated until day 816 when a NaCl solution was infiltrated through three of the nine infiltration panels. This tracer pulse was followed by a potable water flush starting on day 1042. The second tracer experiment began on day 1095 and ended on day 1180. A final potable water flush ended on day1237.

	Potable Water Average Flux (cm/day)	Tracer Water Average Flux (cm/day)	Total Average Flux (cm/day)	Potable Water Standard Deviation	Tracer Water Standard Deviation
Pre Salt Pulse 1	3.01	0.00	3.01	0.16	0.00
Salt Pulse 1	1.92	0.97	2.89	0.10	0.083
Pre Salt Pulse 2	2.81	0.00	2.81	0.18	NA
Salt Pulse 2	1.98	1.05	2.94	0.13	0.15
Post Salt Pulse 2	2.88	0.00	2.88	0.12	NA

Table 1: Average and standard deviations from the flux data plotted in Figure 8.

Neutron data were collected in each one of the 13 PVC cased access wells shown in Figure 3 down to a depth of 12 meters. All data were converted to moisture content through a linear calibration equation developed during the previous EMSP project (Brainard 2003 and Paprocki 2000). The repeatability error for the neutron probe was determined to be ±0.003 by calculating the standard deviation of the several readings taken at one depth in the center access tube over a short period of time. A slightly higher standard deviation of 0.004 was obtained the 3.25 depth in a series of profiles taken at different times. The fact that the standard deviation in measurements taken at the 3.25-meter depth is just slightly larger than the repeatability error for the probe suggests that the larger variations in flux rate did not translate into comparable deviations in subsurface moisture content.

Water samples were collected from the suction lysimeters from Experimental day 500 to Experimental day 1237. Samples were also obtained from the tracer supply tank and occasionally from the potable water supply tank. All samples were analyzed to obtain the electrical conductivity (EC) of the solution. Lysimeter results were inconclusive with the majority of the positions showing a decrease rather than increase in conductivity over time. Lack of correlation to other subsurface estimates of electrical conductivity suggest that the inability of the lysimeters failed to capture infiltrated fluid solutions from the medium surrounding the samplers.

Electrical conductivity (EC) logs collected during the first salt pulse were suspect due to calibration issues that were resolved prior to starting the second salt pulse. A time series of EC profiles obtained during and after the second salt pulse were used to develop three-dimensional images of the developing tracer plume and the attenuation of the plume during the subsequent potable water flush and redistribution after infiltration ceased. To validate the use of EC profiles for obtaining accurate 3-D images of the infiltrated tracer, Hall (2003) compared a series of mass balance calculations using a model developed by Rhoades et al. (1989) with the known infiltrated tracer mass. This model relates bulk soil electrical conductivity to volumetric water content and the electrical conductivity of the soil water. Agreement between the calculated and measured tracer mass suggests that EC profiles can be used to develop 3-D images that at least roughly capture the extent and concentration of the tracer at the STVZ. This research was presented at the Fall AGU meeting (Hall et al, 2003) and will be submitted in article form to a peer-reviewed journal. A plot showing EC profiles from the center access tube collected during and after the second tracer pulse is presented in Figure 9.

Figure 10 shows 3D ERT images of the percent change in estimated subsurface conductivity generated by the saline tracer relative to the background image (Figure 5), Figure 11 a series of 3-D plots derived from interpolation of the EM-39 EC logs from all access tubes, and Figure 12 the associated changes in attenuation from the XBGPR measurements along with images of moisture content. These attenuation images also have the corresponding induction log data plotted coincident to provide additional checks on the imaging results. The tracer solution is about 15 times as conductive as the irrigation water added to the site, and the conductivity of the tracer itself is higher than the conductivity of the residual pore-water in the background of the site.

During the first eight weeks of injection, the ERT images (Figures 10a – 10d) and EM-39 generated images show the tracer tends to move downward along somewhat narrowed pathways, then expand laterally along three separate layers. After the injection of the tracer was stopped, the injection of fresh water continued at the surface and thus the tracer continued moving downward and out of the western edge of the image region; this is shown in last plot in Figure 11 At the surface the size of the conductive region decreases substantially (Figure10f) but still extends to the center of the infiltrometer.

Due to the closer separation of the boreholes and denser sensor spacing used to make the XBGPR measurements, the 2D images shown in Figure 12 provide somewhat higher resolution compared to the ERT images in Figure 10 except in the upper 1.5m where the XBGPR method fails due to refraction of first arrivals along the earth-air interface. Note that the images show the development of a very complicated pattern of solute transport, the accuracy of which is supported by the corresponding induction log data. The results suggest the formation of preferential transport pathways. A closer comparison of the attenuation differences with the moisture content images shows that the regions of higher attenuation difference corresponding to regions of higher moisture content. Because these are unsaturated conditions, this would suggest preferential solute transport through the finer grained materials.

A second possible explanation is that the increase in attenuation within the high moisture content region is caused by a ‘trapping’ of the cations in solution by the finer grained materials. It is well know that

finer grained materials, and especially clays, are more conductive than surrounding coarse grained materials due weakly the presence of cations that are weakly bound adjacent to mineral surfaces due to an inherent negative charge on the clay particles. An increase in cation concentration could conceivable lead to an increase of cations in these weakly bound layers. This idea is supported by background images for the two different salt infiltration experiments that show that the attenuation within the clay regions is higher just prior to the second salt-water tracer test compared to prior to the first salt-water infiltration, even though the system was flushed with pure tap water for 2 months prior to the latter event. This suggests that the excess cations have not been flushed out of the clay which supports the hypothesis of a lack of flow through the clay zones.

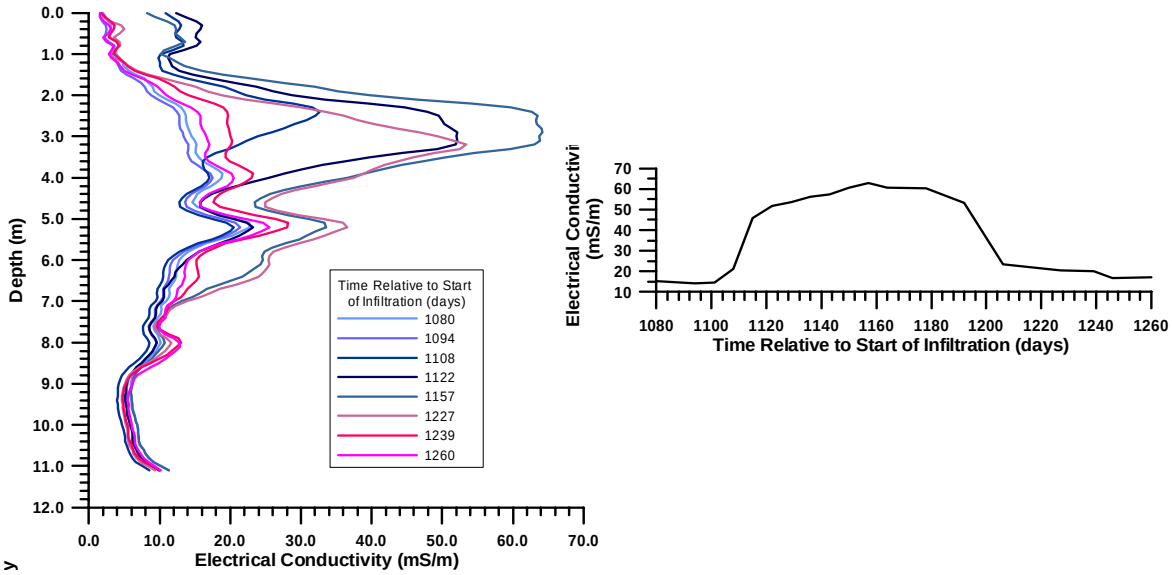

Figure 9: Electrical conductivity profiles obtained from EM39 measurements taken in the center access tube (left graph) and a time series plot of the same data collected at 3.25-meters below the ground surface (right graph). The data starts just before the start of the second tracer pulse and continues through the subsequent tracer water flush and into the redistribution period after infiltration at the site ceased.

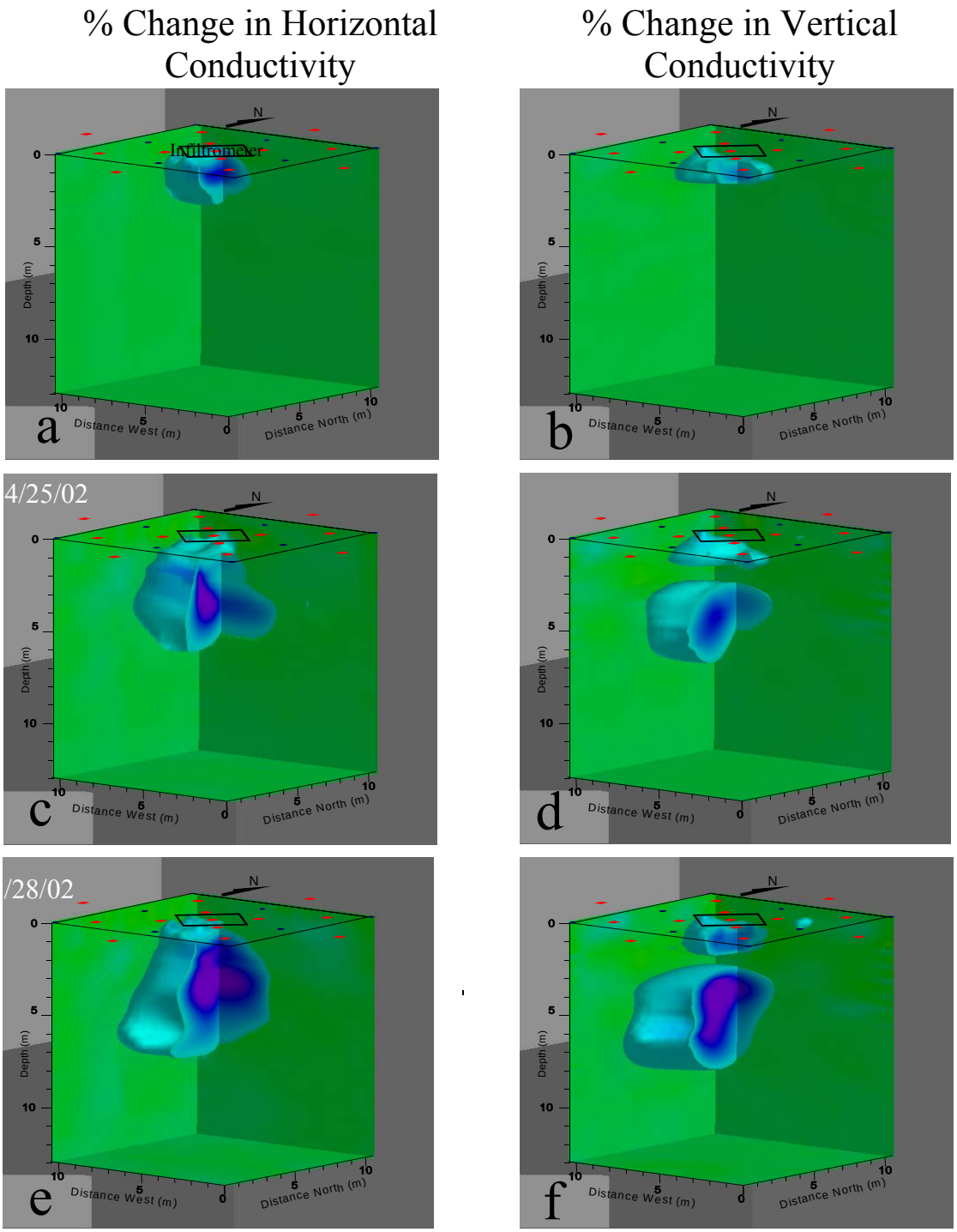

Figure 10: Images of percent change from background of horizontal (a, c, e) and vertical (b, d, f) conductivity caused by the addition of a saline (6900 ppm NaCl solution) through 1/3 of the infiltrometer at the Sandia/Tech vadose zone site. The uppermost row of images (a, b) show changes after two weeks of saline injection. The remaining images are at 1 month intervals.

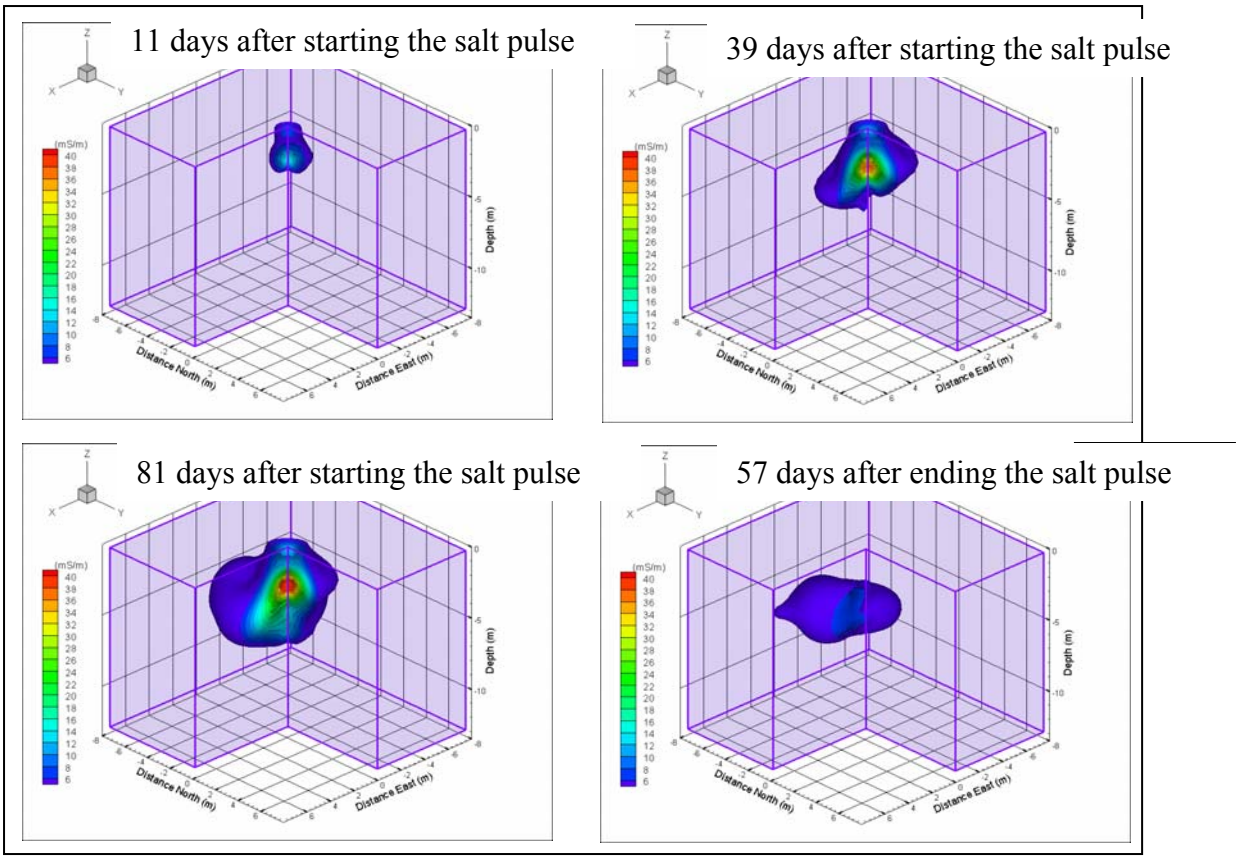

Figure 11: Series of 3-D images of interpolated EM-39 conductivity showing the trace plume development during and after the second salt pulse. The images represent almost a full cycle of plume development during salt infiltration as well as attenuation during the final potable water flush./redistribution.

3.5 Conclusions

The research completed under this project has made significant advances in better understanding transport processes within the vadose zone. It has involved theoretical developments to better include and account for subsurface heterogeneity in both hydrologic and geophysical properties, as well as a field scale experiment using controlled infiltration along with geophysical imaging. New field testing methodologies have been both theoretically developed as well as implemented, and are now ready for testing and deployment at DOE sites. In addition, a database containing all of the pertinent data collected during the experiments is under development; this will be available for use to calibrate predictive models.

The importance of certain findings within this research, however, is currently unknown. For example, is the electrical anisotropy in the various resistivity images related to hydrologic properties, and possibly hydraulic property anisotropy? In addition, without additional data we are unable to distinguish if the complicated pattern that appears in the GPR images is due to preferential transport pathways, or to cationic capture within clay zones. Finally, detailed numerical modeling needs to be completed to determine the image resolution of the geophysical data for recovering images of flow and transport processes. These are all interesting topics for future research, with the latter currently being investigated under an existing EMSP project.

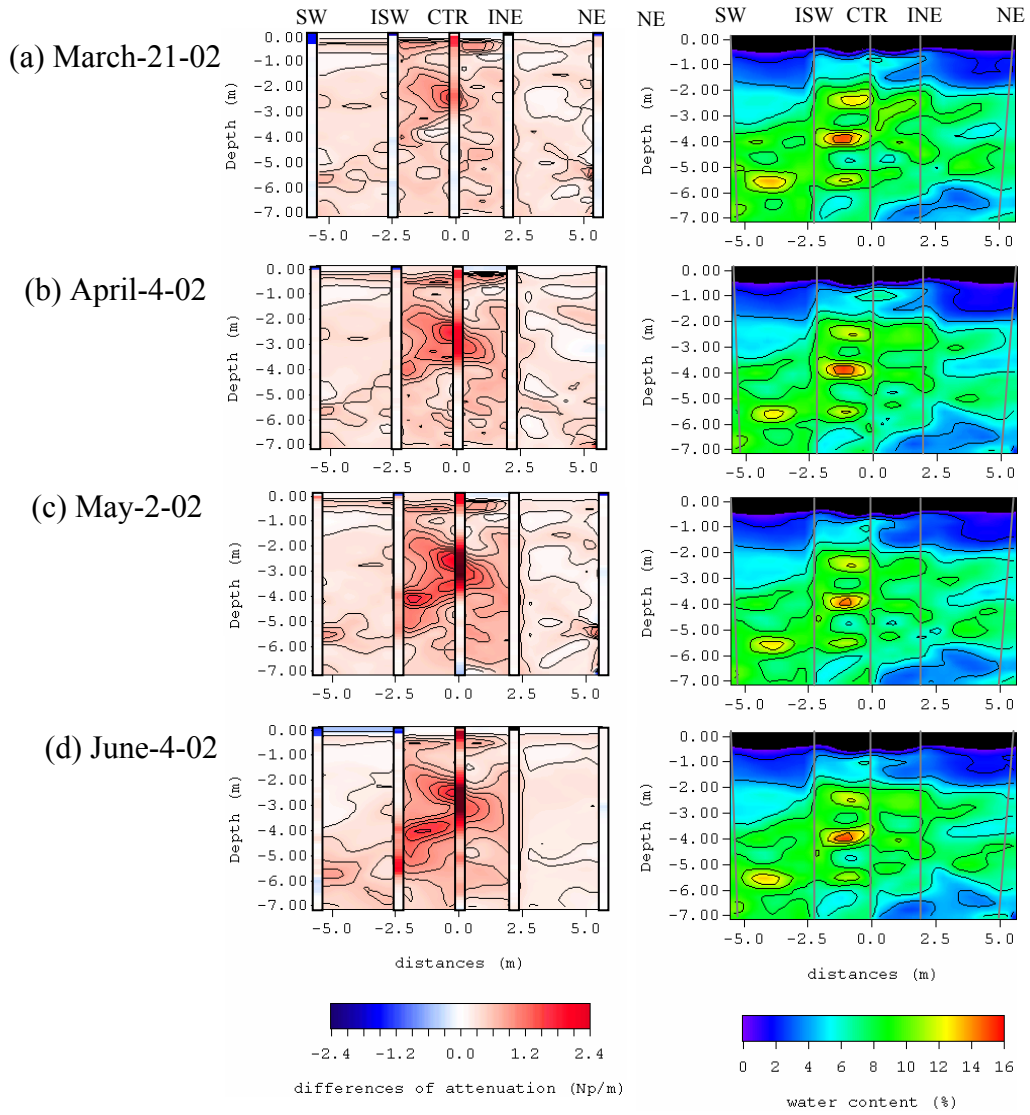

Figure 12: XBGPR derived images of change in attenuation from background (left side) and total moisture content (right side) during the addition of a saline (6900 ppm NaCl) solution through 1/3 of the infiltrometer at the Sandia/Tech vadose zone site.

3.6 Appendix A – ERT Basics

5.6.1 ERT Occam's Inversion Approach for Anisotropic Media

Occam's inversion seeks to find the smoothest possible solution that still fits the data within a specified a-priori value (LaBrecque et al., 1999). An iterative approach is used in which a series of linear approximations are used to search for a solution to the nonlinear inverse problem. Each iteration starts by comparing the data with a forward solution, the numerical approximation of Equation (2). An anisotropic version of the finite-difference formulation of Dey and Morrison (1979) is used to solve for the potentials at a pair of receiver electrodes given within a 3-D anisotropic earth. This formulation uses the simplified form of anisotropy in Equation (3). A conjugate-gradient routine with a symmetric successive-over-relaxation (SSOR) preconditioner is used to solve the linear system of equations for the forward problem (Spitzer, 1995).

The objective function minimized using Occam's inversion is given by

$$\mathbf{S}(\mathbf{m}) = (\mathbf{d}_{\text{obs}} - \mathrm{g}(\mathbf{m}))^{\mathrm{T}}\, \mathbf{W}_{\mathrm{D}}\, (\mathbf{d}_{\text{obs}} - \mathrm{g}(\mathbf{m})) + \alpha\, \mathbf{m}^{\mathrm{T}} \mathbf{R} \mathbf{m}\,, \tag{A-1}$$

where **d** is the vector of data values, **m** is the vector of parameters, **g**(m) is the forward solution, $\mathbf{W}_{\mathrm{D}}$ is the diagonal data weight matrix, **R** is the regularization operator which is discussed in more detail below, and $\mathbf{d}_{\text{obs}}$ is the vector of observed data. α is an empirical factor that controls the amount of regularization versus the fit of the forward model to the data. Minimizing the objective function for a large value of α results in a smooth solution but a poor data fit. The optimal solution corresponds to the largest possible value of α which still fits the data to some a-priori value. LaBrecque et al. (1999) discuss a method of iteratively determining α for 3-D inversion. In the new algorithm, the parameters, **m**, are the natural logarithms of the three components of conductivity (X, Y, and Z) of each cell in the finite-difference mesh.

The nonlinear iterations can be expressed as $\mathbf{m}_{n+1} = \mathbf{m}_n + \Delta\mathbf{m}_n$. The parameter change vector at n^{th} iteration, $\Delta\mathbf{m}_n$, is obtained by solving the linear system

$$\left(\mathbf{G}_n^{\mathrm{T}} \mathbf{W}_{\mathrm{D}} \mathbf{G}_n + \alpha \mathbf{R}\right) \Delta\mathbf{m}_n = \mathbf{G}_n^{\mathrm{T}} \mathbf{W}_{\mathrm{D}} \left(\mathbf{d}_{\text{obs}} - \mathrm{g}(\mathbf{m}_n)\right) - \alpha \mathbf{R} \mathbf{m}_n\,, \tag{A-2}$$

where the elements of the sensitivity matrix, $\mathbf{G}^{\mathbf{T}}$, are given by

$$\mathrm{G}_n^{ij} = \left.\frac{\partial \mathbf{g}^i(\mathbf{m})}{\partial \mathrm{m}^j}\right|_{m_n}. \tag{A-3}$$

The system of equations given by Equation (A-2) is positive-definite and is solved using the conjugate-gradient method with a diagonal preconditioner (LaBrecque et al., 1999). A data-error reweighting scheme is implemented to suppress the effects of data outliers (Morelli and LaBrecque, 1996).

The choice of the regularization operator is critical to the success of the inverse algorithm. The regularization operator can be written in the general form:

$$\mathbf{R} = \mathbf{X}^{\mathbf{T}}\mathbf{X} + \mathbf{Y}^{\mathbf{T}}\mathbf{Y} + \mathbf{Z}^{\mathbf{T}}\mathbf{Z} + \mathbf{M}^{\mathbf{T}}\mathbf{M}\,, \tag{A-4}$$

where $\mathbf{X}^{\mathbf{T}}\mathbf{X}$, $\mathbf{Y}^{\mathbf{T}}\mathbf{Y}$, and $\mathbf{Z}^{\mathbf{T}}\mathbf{Z}$ matrices are used to control the roughness in the X, Y and Z directions respectively and $\mathbf{M}^{\mathbf{T}}\mathbf{M}$ is used to minimize the anisotropy. Although there are a number of possible choices for this regularization operator, the regularization operator used for all of the results presented in this paper measures/controls the roughness of the mean of the parameters. Since the parameters are the natural logs of the conductivity, the operator forces the geometric mean of conductivity to be smooth. The $\mathbf{X}^{\mathbf{T}}\mathbf{X}$, $\mathbf{Y}^{\mathbf{T}}\mathbf{Y}$, and $\mathbf{Z}^{\mathbf{T}}\mathbf{Z}$ matrices are sparse and symmetric. They are assembled by adding together blocks where each block measures the roughness between a pair of adjacent elements within the finite-

difference mesh. For example, for a pair of elements i, and i+1, the corresponding block for the regularization operator would have the form:

$$a_i \cdot \begin{array}{c} \begin{matrix} X_i & Y_i & Z_i & X_{i+1} & Y_{i+1} & Z_{i+1} \end{matrix} \\ \begin{bmatrix} 1 & 1 & 1 & -1 & -1 & -1 \\ 1 & 1 & 1 & -1 & -1 & -1 \\ 1 & 1 & 1 & -1 & -1 & -1 \\ -1 & -1 & -1 & 1 & 1 & 1 \\ -1 & -1 & -1 & 1 & 1 & 1 \\ -1 & -1 & -1 & 1 & 1 & 1 \end{bmatrix} \end{array} \begin{matrix} X_i \\ Y_i \\ Z_i \\ X_{i+1} \\ Y_{i+1} \\ Z_{i+1} \end{matrix}, \qquad \text{(A-5)}$$

where a_i is a weight applied to the entire block. In the example above, X_i, Y_i, Z_i, are included to indicate the rows and columns of the block corresponding to the X, Y, and Z components of the i^{th} element. The values of the weights are varied following a scheme discussed by Morelli and LaBrecque (1996).

The $\mathbf{M}^T\mathbf{M}$ matrix acts on individual elements and is assembled in a similar fashion. For element i, the corresponding block for the $\mathbf{M}^T\mathbf{M}$ matrix is:

$$a_i \cdot \begin{array}{c} \begin{matrix} X_i & Y_i & Z_i \end{matrix} \\ \begin{bmatrix} 2 & -1 & -1 \\ -1 & 2 & -1 \\ -1 & -1 & 2 \end{bmatrix} \end{array} \begin{matrix} X_i \\ Y_i \\ Z_i \end{matrix}. \qquad \text{(A-6)}$$

3.6.2 ERT Field Methodology

Eight vertical electrode arrays (VEAs), each containing 17 copper electrodes spaced at 76 cm intervals were deployed at the corners of two concentric squares. The first square was 12 meters on a side the smaller square was 4 meters on a side and was rotated 45 degrees with respect to the first square. The uppermost electrode is just below the surface, while the lowest is 12 m deep. In addition to the eight VEAs, in the central portion of the site, the ERT data collection used 32 electrodes placed just below the surface. Finally there are two reference electrodes placed as far from the center as practical, 19.9 m northwest and 19.9 m southeast of the center of the infiltrometer.

The ERT data collected in this study consisted of pseudo-pole-pole data. True pole-pole data requires a pair of reference electrodes, one for potential measurements and one for current injection, to be placed a large distance (relative to the scale of the site) away from the measurement region. For this site, the distance from the site to the reference electrodes is fairly small (about 20 meters), so the data were not truly pole-pole and the locations of the poles significantly affected the measured values. For every data point we collected a reciprocal measurement, ie. the measurement in which the transmitting and receiving electrode pairs are interchanged.

At this site, we collected 29,412 reciprocal pairs, a total of 58,824 data values. This required a minimum of about 14 hours to collect, thus data collection was often spread over a two-day period. In theory, reciprocal measurements should yield nearly identical results, thus reciprocals provide an excellent method of assessing the noise within the data. Each data point is compared with its reciprocal. Data in which the two reciprocal data points agreed within 5% were averaged together and retained; the remaining data were removed from the inversion input. Generally about 95% of the data were retained, yielding about 28,000 averaged data values. The results were inverted using the 3-D anisotropic algorithm described by LaBrecque and Casale (2002). The code also implements a differencing inversion scheme similar to that

described by LaBrecque and Yang (2001) to allow effective imaging of small changes in background resistivity. Both of these improvements to the 3-D code produce images less prone to noise and inversion artifacts and more robust with respect to individual starting models.

The region to be imaged was discretized into a mesh of 44 × 44 × 40 = 77,440 elements. Element size ranged from .38 m in the center of the mesh to 6 m along the boundaries. The inversion of a complete background data set took about 9 hours on a Pentium 4, 1.8 GHz PC.

3.7 Appendix B – XBGPR Basics

3.7.1 GPR General Theory

A GPR system transmits a pulse of electromagnetic energy, with a center frequency ranging from 10 MHz to 1GHz, which propagates through subsurface soils or rock. For many common unsaturated soil and rock materials, the conductivity is less than 10 mS/m (Davis and Annan, 1989). Thus, the velocity of the electromagnetic wave propagating through such materials can be approximated as:

$$v \approx \frac{c}{\sqrt{k_a}} \qquad \text{(B-1a)}$$

and the attenuation is

$$\alpha \approx \frac{1}{2}\sqrt{\frac{\mu_0}{\varepsilon_0}}\frac{\sigma}{\sqrt{k_a}}. \qquad \text{(B-1b)}$$

In equation (B-1a), the parameter c is the velocity of light in a vacuum,

$$c = \frac{1}{\sqrt{\varepsilon_0 \mu_0}} = 3 \times 10^8 \, m/s \ , \qquad \text{(B-2)}$$

where ε_0, μ_0 are the dielectric permittivity (8.85×10^{-12} F/m) and magnetic permeability ($4\pi\times10^{-7}$ H/m) in free space, respectively. σ is the electrical conductivity of the medium. k_a is the dielectric constant and is given by

$$k_a = \frac{\varepsilon}{\varepsilon_0} \text{ (e.g. } k_a\text{=1 in air; and } k_a\text{=80 in pure water)}, \qquad \text{(B-3)}$$

where ε is the dielectric permittivity of the medium.

In equation (B-1a) and (B-1b), the radar wave velocity depends on the dielectric constant, and the attenuation is subject to both dielectric constant and conductivity of the medium. The presence of water and clay minerals in a porous medium will tend to increase the dielectric constant and conductivity.. Topp and his colleagues derived an empirical expression (Topp et. al, 1980)

$$\theta = -5.3\times10^{-2} + 2.9\times10^{-2} k_a - 5.5\times10^{-4} k_a^2 + 4.3\times10^{-6} k_a^3 \qquad \text{(B-4a)}$$

by measuring the dielectric constant of sediments of variable water saturation using time-domain-reflectometry (TDR). The equation describes the relationship of water content, θ, to the dielectric constant, k_a. Due to the presence of iron oxide minerals at the test site, Alumbaugh et al. (2002) suggested an empirical equation

$$\theta = 0.0136 k_a - 0.033 \qquad \text{(B-4b)}$$

for the relationship of water content to TDR-measured dielectric constant at the STVZ site. By applying equation (B-1a) and (bB-4b), water content can be estimated from EM wave velocity, and this method has been used to tomographically image moisture content between two boreholes (e.g. Alumbaugh et al., 2000; Alumbaugh et al., 2002; Binley et al., 2001; LaBrecque et al., 2002; Hubbard, 1997[b]).

3.7.2 XBGPR Data Acquisition System and Configuration

A Sensors and Software PulseEKKO 100 GPR system was employed to obtain the cross-borehole measurements. GPR data were collected using Multi-Offset Gathers (MOG's) with antenna frequency of 100 MHz (Figure 4). Data were acquired by positioning the transmitting antenna within a borehole, and collecting data at several receiver depths in another borehole a few meters away. The angle of the line connecting the transmitting antenna and the receiving antenna and the horizontal was limited to 45 degrees in order to avoid influences of wave reflections from high angles of antenna offset (Peterson, 2001), low signal-to-noise ratios at high angles, and problems with the presence of wires within the ground (Paprocki, 2000; Alumbaugh et al., 2002). XBGPR data were collected in 0.25-m increments along the adjacent boreholes located on the aforementioned survey line (Figure 3) from 0 to 12 m depth. Data for the four well pairs, SW-ISW, ISW-CTR, CTR-INE and INE-NE, were combined and processed together to present tomographic images along an 11-m long profile. The separations of SW-ISW, ISW-CTR, CTR-INE and INE-NE were 3.04 m, 2.4 m, 2.25 m and 3.25 m, respectively.

To track any fluctuations in the GPR transmitter output during data collection, a time-zero calibration was conducted every ten transmitter depths. This involves placing the transmitting and receiving antenna a known distance apart in the air, which allows the user to determine the arrival time and to correct for system error. In addition, time-zero calibration also allows us to check the consistency of the amplitude data during the time-lapse measurements.

First-arrival time (travel time) and amplitude of the received EM signals are used as data to invert for velocity and attenuation. For this experiment, the inversion domain consists of a discrete 2D grid of cells that are 0.25m on both sides. The travel time and attenuation for each GPR "time-series" first arrival can be represented as (Sharma, 1997; Jackson & Tweeton, 1996):

$$t_i(or\ \alpha_i) = \sum_{j=1}^{M} p_j d_{ij} \qquad \text{(B-5)}$$

where $t_i(\alpha_i)$ represents the total travel time or attenuation for the i^{th} ray path, p_j is the average slowness or attenuation of the j^{th} cell, d_{ij} is the distance of the i^{th} ray path within the j^{th} cell, and M represents the number of cells passed through by the i^{th} ray path. The attenuation of each ray path can be calculated as:

$$\alpha_i = -\ln \frac{A_i}{A_0}, \qquad \text{(B-6)}$$

where A_0 is the amplitude of the transmitted wave form, and A_i is the received amplitude.

Unfortunately, it is impossible to measure the transmitter amplitude, A_0, directly. Here we employed GPR signals collected at receiver positions ranging from 7 to 10 m depth, with transmitter positions from 9 to 10 m beneath the surface to back-calculate the transmitter amplitude using the process described below. From the core records, the soil between 7 and 10 m is a relatively homogeneous sand, and therefore an EM wave propagating through it can be assumed to travel as a straight ray. Because the amplitude attenuates exponentially along the ray path, A_0 can then be estimated by performing an exponential regression of the amplitude against the length of the ray path. Care should be taken when using an entire XBGPR data set for the A_0 estimation, because the presence of heterogeneous structures will result in an inaccurate transmitter amplitude estimate (Peterson, 2001).

Factors other than intrinsic attenuation, including geometrical spreading and the radiation pattern of the transmitter and receiver, also affect the amplitude measured by the GPR system (Peterson, 2001). The transmitting antenna can be thought of as a dipole that radiates EM waves in a spherical geometry. Thus the measured amplitude in a homogeneous medium can be represented as:

$$A_m = A_i(\cos\theta / R), \qquad \text{(B-7)}$$

where A_i is the amplitude that only depends on the intrinsic attenuation for the i^{th} ray path, θ is the angle measured from the horizontal to the ray path, and R is the distance between the transmitter and receiver antennas.

The corrected amplitudes of the EM waves measured in the thick sand section are shown in Figure B-1(a). In a homogenous media, the amplitudes corrected for spherical spreading and radiation pattern will decrease exponentially along the ray path. However, Figure B-2(a) shows that the normalized amplitude does not appear to be exponentially related to the antenna distance, and several clusters of data corresponding to different well pairs are apparent.

Peterson (2001) suggests that using a third order radiation pattern, $\cos^3\theta$, can suppress the clusters and yield a better correlation to the regression curve. However, as shown in Figure B-1(b), the use of a third order radiation pattern to normalize the data does not eliminate clusters of data. This suggests that for this data set, the clusters may be originating from incorrect antenna positions or well orientations, and therefore these effects should be taken into account. If the boreholes were normal to the surface, the amplitude normalized by equation (B-7) should exponentially decay with ray path distance. However, if the borehole deviates from vertical but the data are treated assuming a vertical borehole, clusters corresponding to different well pairs will appear in a graph of amplitude versus ray path distance.

Since the deviation angles of the boreholes were not measured, one way to estimate if a correction is required is to perturb the position of borehole bottom slightly and constrain the tilt angle to a maximum of 5 degrees until a better correlation to the regression curve is achieved. The two center well pairs were found to overlap when plotted together and therefore the three inner wells were assumed to be vertical. Thus the deviation correction was made only for two outer boreholes, NE and SW, and the optimal deviation of the bottom for boreholes NE and SW are found to be 50cm and 18cm, respectively. The results after corrections of borehole deviation yield better correlation of the normalized amplitude to the regression curve (Figure B-1(c)), and thus this correction process is employed in the processing procedure prior to inverting the data.

The inversion code, GeotomCG^{TM} (GeoTom,LLC, 1998), was used to produce images of velocity and attenuation from travel time and normalized amplitude measurements. GeotomCG^{TM} employs a simultaneous iterative reconstruction technique (SIRT) (Jackson & Tweeton, 1996) and ray tracing methods to generate tomographic images. Straight ray inversion, which assumes the ray path between the transmitter and receiver is a straight line, was chosen for both velocity and attenuation inversion. Theoretically, the first arriving EM wave-fronts tend to travel through high-velocity regions rather than low-velocity regions. This makes the ray paths in an inhomogeneous medium tend to curve around the low-velocity regions and thus they are no longer straight lines. Although it may be more accurate to use curved ray inversion (Alumbaugh et. al, 2002), the difficulty of estimating A_0, the correction factor for geometric spreading, and the antenna radiation made the curved ray attenuation inversion difficult to apply. Therefore, straight ray inversion was adopted to generate velocity and attenuation tomograms in this study. Because we are interested in the attenuation changes associated with the water infiltration in the heterogeneous soils, we only processed data to 7 m depth, since from 7 to 10 m depth the soil is mainly composed of homogenous fine sand.

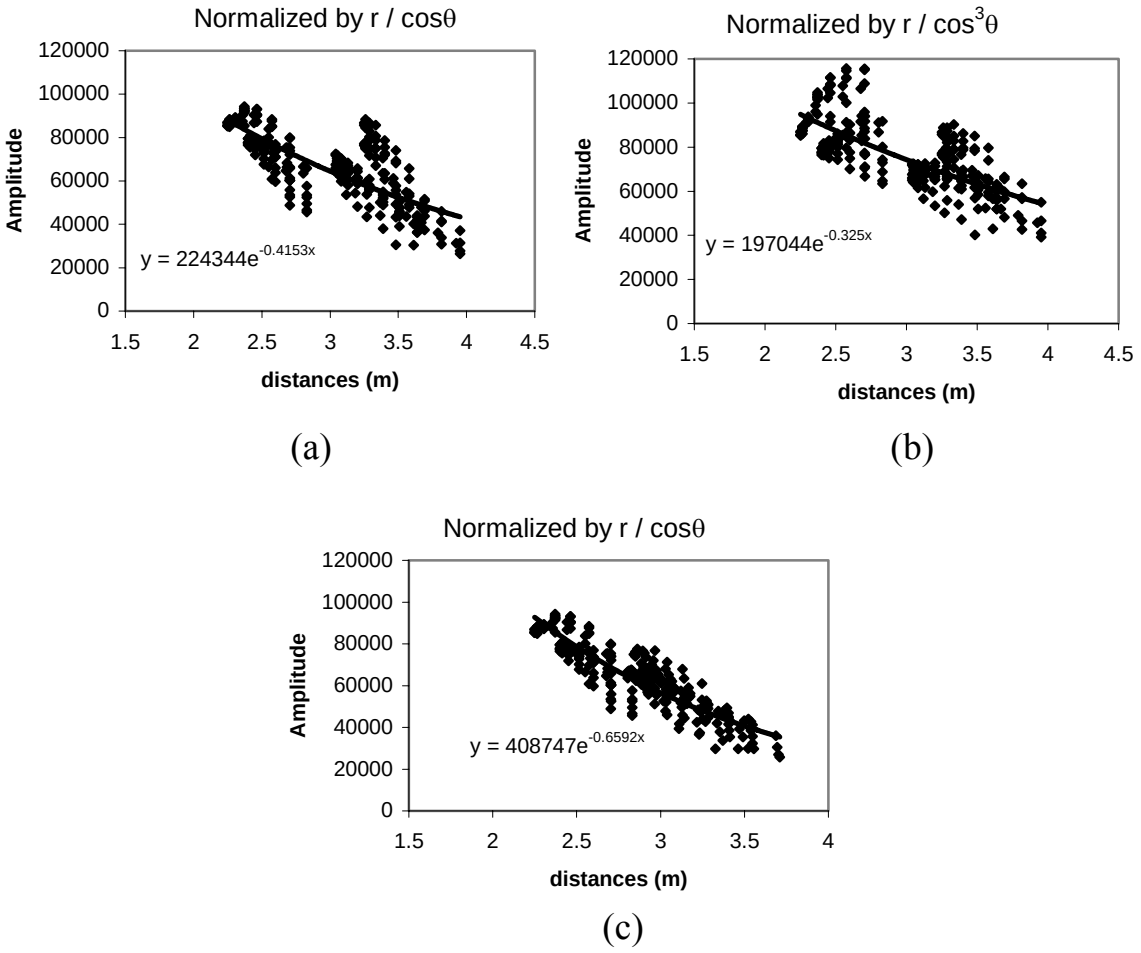

Figure B-1. Plots of normalized amplitude versus source–receiver separation for transmitter antenna located in sand layer at 9 to 10m, and the corresponding regression curves. (a) Without correction for tilting of boreholes, amplitudes are normalized by r/cosθ̃ (b) Without correction for tilting of boreholes, amplitudes are normalized by r/cos^{3}θ̃ (c) With correction for the borehole deviation, amplitudes are normalized by r/cosθ̃

3.8 References

Alumbaugh, D., Paprocki, L., Brainard, J., Rautman, C., 2000, Monitoring infiltration within the vadose zone using cross borehole ground penetrating radar, In: Proceedings of the symposium on the Application of geophysics to engineering and environmental problems, pp. 273-281, Environmental and Engineering Geophysical Society. Wheat Ridge, CO, United States.

Alumbaugh, D., Chang, P. Y., Paprocki, L., Brainard, J. R., Glass, R. J., Rautman, C. A., 2002, Estimating moisture contents using cross-borehole ground penetrating radar; a study of accuracy and repeatability in context of an infiltration experiment, Water Resource Research 38 (12), 45-1-45-12.

Archie, G.E., 1942. Electrical resistivity log as an aid in determining some reservoir characteristics: Am. Inst. Mining and Metal. (Engr. Transl.), **146**, pp. 54-62.

Binley, A., Winship, P., Middleton, R., Pokar, M., West, J., 2001, High-resolution characterization of vadose zone dynamics using cross-borehole radar, Water Resource Research 37 (11), 2639-2652.

Brace, W. F., 1977, "Permeability from resistivity and pore shape", Journal of Geophysical Research, **82**, pp. 3343-3349.

Brainard, J. R., R. J. Glass, D. L. Alumbaugh, L. Paprocki, D. J. La Brecque, X. Yang, T.-C. J. Yeh, K. E. Baker and C. A. Rautman. 2003. The Sandia-Tech Vadose Zone Facility; experimental design and data report of a constant flux infiltration experiment. Sandia Internal Report – Sand Document. Sandia National Laboratories, Albuquerque, N.M.

Brainard, J. R., D. L. Alumbaugh, D. J. La Brecque, T. –C. J. Yeh, P.-Y. Chang, and L. M. Hall. 2004. The Sandia-Tech Vadose Zone Facility, experimental design and data report of tracer experiments. Sandia Internal Report In Progress. Sandia National Laboratories, Albuquerque, NM.

Chang, P. Y., D. L. Alumbaugh, J. R. Brainard, and L. Hall, 2003a, The application of ground penetrating radar attenuation tomography in a vadose zone infiltration experiment, Accepted by Journal of Contaminant Hydrology

Davis, J., L., and Annan, A., P., 1989, Ground-penetrating radar for high-resolution mapping of soil and rock stratigraphy, Geophys. Prosp., 37, 531-551.

Davis, J.M., Wilson, J.L., and Phillips, F. M., 1994, A portable air mini-permeameter for rapid in-situ field measurments; Groundwater, **32**(2), 258-266.

Dey, A. and Morrison, H.F., 1979, Resistivity modeling for arbitrarily shaped three-dimensional structures: Geophysics, 44, 753-780.

DOE report, Goundwater/Vadose Zone Intergration Project Specification (DOE/RL-98-48) – Draft C.

General Accounting Office, 1998, Understanding of Waste Migration at Hanford is Inadequate for Key Decisions GAO Report GAO/RCED-98-80.

GeoTom, LLC.,1998, User Mannual for GeotomCG and GeoTom3D, GeoTom, LLC., Apple valley, Minnesota.

Hall, L, M. 2003. Measuring Salinity Changes in the Vadose Zone Using Down-hole Electromagnetic Induction. [M.S. Thesis]: Department of Geoscience, New Mexico Institute of Mining and Technology, Socorro, New Mexico, 259 p.

Hall, L. M., J. R. Brainard, R. S. Bowman, J. H. Hendrickx. 2003. Determination of Solute Distributions in the Vadose Zone Using Down-hole Electromagnetic Induction. *Eos Trans. AGU, 84(46)*, Fall Meet. Suppl., Abstract.

Hubbard, S. S., Peterson, J. E., Majer, E., Zawislanski, P. T., Williams, K.H., Roberts, J., Wobber, F., 1997[b], Estimation of permeable pathways and water content using tomographic radar data, The Leading Edge, 16 (11), 1623-1628.

Hughson, D. L. and T.-C. J. Yeh, An inverse model for three-dimensional flow in variably saturated porous media, Water Resources Research, 36(4), 829-839, 2000.

Jackson, M., J., Tweeton, D., R., 1996, 3DTOM: Three-dimentional geophysical tomography, Report of investigations 9617, Bureau of Mines, United Stated Department of the Interior., pp. 1-84.

Keller, G. V. and Frischknecht, F. C., 1966, Electromagnetics Methods in Geophsysical Prospecting, Chapter 3, Pergamon Press, 517 p.

Kunz, K. S. and Moran, J. H., 1958, Some effects of formation anisotropy on resistivity measurements in boreholes: Geophysics, **23**, 770-794.

LaBrecque, D., Alumbaugh, D., L., Yang, Y., Paprocki, L., Brainard, J., 2002, Three-dimensional monitoring of vadose zone infiltration using electrical resistivity tomography and cross-borehole

ground penetrating radar, Three-dimentional electromagnetics, Methods in Geochemistry and Geophysics, 35, p. 260-272, Elsevier, New York.
LaBrecque, D. J., Morelli, G., Daily W., Ramirez, A., and Lundegard, P., 1999, Occam's Inversion of 3D ERT data: in: Spies, B., (Ed.), Three-Dimensional Electromagnetics, SEG, Tulsa, 575-590.
LaBrecque, D. J., and Yang, X., 2001, Difference inversion of ERT data: a fast inversion method for 3-D in-situ monitoring: Journal of Environmental and Engineering Geophysics, **6**, 83-90.
LaBrecque and Casale, 2002, Experience with Anisotropic Inversion for Electrical Resistivity Tomography, Proceedings of the Symposium on the Application of Geophysics to Engineering and Environmental Problems (SAGEEP) '02.
Liu, S., and T. -C. J. Yeh, Effectiveness of Hydraulic Tomography: Sandbox Experiments, Eos Transactions AGU, 82(47), Fall Meeting Supplement, Abstract H21A-2086, 2001
Liu, S., T. -C. J. Yeh and R. Gardiner, Effectiveness of hydraulic tomography: Sandbox experiments, Water Resources Research, 38(4), Art. No. 1034, doi:10.1029/2001WR000338, 2002.
Liu, S. and T.-C. J. Yeh, An integrative approach for monitoring water movement in the vadose zone, Vadose Zone Journal, accepted for publication, 2004.
Morelli, G., and LaBrecque, D. J., 1996, Robust scheme for ERT inverse modeling: European Journal of Environmental and Engineering Geophysics, **2,** 1-14.
Nelson, P.H., and Hearst, J.R., 1985, Well Logging for Physical Properties: McGraw-Hill, 571p.
Paprocki, L. T. 2000, Characterization of vadose zone in-situ moisture content and an advancing wetting front using cross-borehole ground penetrating radar, [M.S. thesis]: Department of Geoscience, New Mexico Institute of Mining and Technology, Socorro, New Mexico, 120 p.
Peterson, J. E., 2001, Pre-inversion Correction and analysis of radar tomographic data, Journal of Environmental & Engineering Geophysics, 6, 1-18.
Rhoades, J.D., N.A. Manteghi, P.J.Shouse, and W.J. Alves. 1989. Soil Electrical Conductivity and Soil Salinity: New Formulations and Calibrations. Soil Sci. Soc. Am.J. 53:433-439.
Sharma, P. V., 1997, Environmental and engineering geophysics, Cambridge university press, New York.
Sheets, K.R., and Hendrickx, J.M.H., 1995, Noninvasive soil water content measurement using electromagnetic induction: Water Resour. Res., **31**, 2401-2409.
Slavich, P.G., and Petterson, G.H., 1990, Estimating Average Rootzone Salinity from Electromagnetic Induction (EM-38) Measurements: Aust. J. Soil Res., **28**, 453-463.
Spitzer, K., 1995, A 3-D finite difference algorithm for DC resistivity modeling using conjugate gradient methods: Geophysical J. Int'l, 123, 903-914.
Yeh, T.-C. J., S. Liu, R.J. Glass, K. Baker, R. Brainard, D. Alumbaugh, and D. LaBrecque, A geostatistically based Inverse method for electrical resistivity surveys and its applications to the vadose zone hydrology, Water Resour. Res., 38(12), Art. No. 1278, 2002.
Vargaas-Guzman, J. A., and T.-C. J. Yeh, The successive linear estimator: a revisit, Advances in Water Resources, 25(7), 773-781, 2002.
Yeh, T.-C. J. and S. Liu, Hydraulic tomography: Development of a new aquifer test method, Water Resources Research, 36(8), 2095-2105, 2000.
Yeh, T.-C. J. and J. Simunek, Stochastic Fusion of Information for Characterizing and Monitoring the Vadose Zone, Vadose Zone Journal, 1, 207-221, 2002.
Yeh, T.-C. J., Stochastic Fusion of Information for Imaging the Vadose Zone – in memory of Professor Allan Gutjahr, Eos Transactions AGU, 83(47), Fall Meeting Supplement, Abstract H61E-05 Invited, 2002.
Zhu, J. and T. -C. J. Yeh, Stochastic Fusion of Information: An application to Monitoring Water Movement in STVZ Infiltration Field Site., Eos Transactions AGU, 83(47), Fall Meeting Supplement, Abstract H61A-0744, 2002.

4.0 Relevance, Impact, and Technology Transfer

This project has analyzed electrical resistivity and cross-borehole ground penetrating radar tomography in terms of their abilities to monitor the movement of tracers and contaminate plumes within the vadose zone. This information has already impacted both the theory and practice of ERT monitoring. Technologies developed or substantially improved during the course of this project include, application of techniques to monitoring small, long-term changes in resistivity, the application of inversion for anisotropic subsurface properties, the development and testing of strategies for long-term monitoring using electrical resistivity tomography, improvement of data collection strategies, the application of temperature corrections to

remove annual temperature changes, and the investigation of methods of estimating subsurface hydrological properties such as saturation. In terms of GPR technology the project has demonstrated what the benefits and limitations are of XBGPR imaging for repeat, long term monitoring of sites. In addition new hydrologic estimation techniques have been developed that may become commonly used by the DOE and other agencies in the future.

The work completed under this project has already impacted the approach to long-term monitoring of enhanced remediation and acid mine drainage with the installation of 600+channel ERT system in South Dakota. Plans are also underway to apply the methods to full-scale three-dimensional ERT monitoring at the Dynamic Underground Stripping remediation site funded by the State of Washington Department of Ecology beginning in December 2003, and at the Savannah River Site in the summer or fall of 2004.

5.0 Project Productivity

The project completed almost all of its goals. Studies were carried out at the site using two different tracer concentrations. The movement of the tracer was successfully monitored using electrical resistivity and XBGPR tomography. The latter required new methods of data analysis including corrections for annual temperature changes. These new methods were applied to data collected during the initial infiltration conducted during a previous study. This allowed a careful comparison of the effects of salinity changes versus changes in subsurface saturation.

Continued improvements were made to the hydrologic property estimation techniques. This included better ways of estimating moisture content from electrical resistivity images. Although some hydrologic modeling of the transport experiment was performed, detailed 3D models were not implemented to the extent that we could compare to the actual transport experiments. This was primarily due to the early realization that we lacked certain soil property measurements such as 'dispersivity' that would allow for meaningful interpretation of the models.

6.0 Personnel Supported

Ping Yu Chang, PhD Student, University of Wisconsin-Madison

Laila Hall, MS Student, New Mexico Technical Institute of Mines and Technology, Supported via Sandia National Laboratories and MultiPhase Technologies, LLC.

S. Liu, A. Wolf, K. Kuhlman, J. Zhu, Students, Department of Hydrology and Water Resources, University of Arizona.

J. A. Vargaas-Guzman, Department of Hydrology and Water Resources, University of Arizona, Postdoctoral fellow.

Melissa Stuben, Geophysicist, Roger Sharpe, Senior Geophysicist, MultiPhase Technologies, LLC.

7.0 Publications

7.1 Theses

Chang, P. Y., 2003, An analysis of a coupled geophysical tomography -hydrological modeling method to characterize hydraulic properties, and flow and transport process in the vadose zone; PhD Thesis, Geological Engineering Program, University of Wisconsin-Madison, Madison, Wisconsin.

Hall, L, M. 2003, Measuring Salinity Changes in the Vadose Zone Using Down-hole Electromagnetic Induction. M.S. Thesis, Department of Geoscience, New Mexico Institute of Mining and Technology, Socorro, New Mexico.

Liu, S.,2002, An integrative approach for monitoring water movement in the vadose zone,Ph.D. Thesis, Department of Hydrology and Water Resources, University of Arizona.

Wolf, A., 2002, A statistical approach to calibrate groundwater flow model,M.S. Thesis, Department of Hydrology and Water Resources, University of Arizona.

Kris Kuhlman, 2004,Adaptive mesh refinement technique for simulation of flow through variably saturated zone, M.S. Thesis, Department of Hydrology and Water Resources, University of Arizona, *in progress*.

Zhu, J.,2004, Stochastic Fusion of Information: An application to Monitoring Water Movement in STVZ Infiltration Field Site, Ph.D. Thesis, Department of Hydrology and Water Resources, University of Arizona, *in progress*.

7.2 Published Peer Reviewed Journal Articles

Alumbaugh, D. L., Chang, P.Y., Paprocki, L., Brainard, J. R., Glass, R. J., and Rautmann, C., 2002, Estimating moisture contents using cross-borehole ground penetrating radar; a study of accuracy, repeatability and resolution in context of an infiltration experiment; *Water Resources Research,* **38,**1309.

LaBrecque, Douglas J., and Yang, Xianjin, 2001, Difference Inversion of ERT data: a fast inversion method for 3-D in situ monitoring: Journal of Environmental and Engineering Geophysics, **6**, 83-90.

LaBrecque, Douglas J., Alumbaugh, David L., Yang, Xianjin, Paprocki, Lee, 2002, Three-Dimensional Monitoring of Vadose Zone Infiltration using Electrical Resistivity Tomography and Cross-Borehole Ground Penetrating Radar: in Zhdanov, M. and Wannamaker, P., (Ed.), Three-Dimensional Electromagnetics II, Elsevier, New York, 259-272.

Liu, S., T. -C. J. Yeh and R. Gardiner, Effectiveness of hydraulic tomography: Sandbox experiments, Water Resources Research, 38(4), Art. No. 1034, doi:10.1029/2001WR000338, 2002.

Vargaas-Guzman, J. A., and T.-C. J. Yeh, The successive linear estimator: a revisit, Advances in Water Resources, 25(7), 773-781, 2002.

Yeh, T. C. J, Liu, S, Glass, R. J., Baker, K., Brainard, J, Alumbaugh, D. L., and Labrecque, D., 2002, A geostatistically-based inverse model for electrical resistivity surveys and its applications to vadose zone hydrology; *Water Resources Research*; **38**, 1278.

Yeh, T.-C. J. and J. Simunek, Stochastic Fusion of Information for Characterizing and Monitoring the Vadose Zone, Vadose Zone Journal, 1, 207-221, 2002.

7.3 Accepted or In Review

Chang, P. Y., Alumbaugh, D., Brainard, J., and Hall, L., 2003, The application of ground penetrating radar attenuation tomography in a vadose zone infiltration experiment; *Journal of Contaminant Hydrology,* In Press.

Chang, P. Y. , Alumbaugh, D. L., Brainard,J, and Hall, L, 2004, Monitoring and imaging of a vadose-zone solute transport experiment using cross borehole ground penetrating radar tomography, Submitted for second review to Water Resources Research.

Daniels, J. J., Allred, B., Binley, A., LaBrecque, D., Alumbaugh, D., 2004, Vadoze Zone Applications: in Rubin, Yoram and Hubbard, Susan, (Ed.) Hydrogeophysics, Kluwer, New York In Pres

LaBrecque, D., Stubben, M., and Hall, L., 2004, Tracking saline tracer in the vadose zone using electrical resistivity tomography, submitted to Water Resources Research.

Liu, S. and T.-C. J. Yeh, 2004,An integrative approach for monitoring water movement in the vadose zone, Vadose Zone Journal, In Press.

7.4 Published in unreviewed publications (proceedings, technical reports,etc.)

Alumbaugh, D. L, Chang, P. Y., LaBrecque, D., Stueben, M., Brainard,J, and Hall, L., 2003 Investigating vadose-zone flow and transport processes using cross borehole GPR and electrical resistivity; *Presented* at *the 2003 Annual Meeting of the Society of Exploration Geophysicists*, October of 2003, Dallas, TX, *Invited*.

Alumbaugh, D. L., LaBrecque, D. , Paprocki, L., Brainard., J., Yang, X., Glass, R. J., Chang, P. Y., 2000, Geophysical monitoring of flow and transport processes within the vadose zone: a resolution, accuracy and precision analysis of electrical resistivity tomography and cross borehole ground penetrating radar**;** Presented at the *2000 American Geophysical Union Annual Fall Meeting*, San Francisco, California.

Brainard, J. R., R. J. Glass, D. L. Alumbaugh, L. Paprocki, D. J. La Brecque, X. Yang, T.-C. J. Yeh, K. E. Baker and C. A. Rautman. 2003. The Sandia-Tech Vadose Zone Facility; experimental design and data report of a constant flux infiltration experiment. Sandia Internal Report – Sand Document. Sandia National Laboratories, Albuquerque, N.M.

Brainard, J. R., D. L. Alumbaugh, D. J. La Brecque, T. –C. J. Yeh, P.-Y. Chang, and L. M. Hall. 2004. The Sandia-Tech Vadose Zone Facility, experimental design and data report of tracer experiments. Sandia Internal Report In Progress. Sandia National Laboratories, Albuquerque, NM.

Chang, P. Y., Alumbaugh, D., Brainard, J., and Hall, L., 2002, Using cross borehole ground penetrating radar attenuation tomography for characterizing soil properties in the vadose zone during a two-stage infiltration test; Presented at *the 2002 Annual Meeting of the Society of Exploration Geophysicists*, September of 2002, Salt Lake City, Utah.

Chang, P. Y., Alumbaugh, D., Brainard, J., and Hall, L., 2002, Characterization of Flow Properties and Processes in the Vadose Zone Using Cross Borehole GPR; Presented at the *16th Workshop on Electromagnetic Induction in the Earth*. Santa Fe, New Mexico, June 16-Jun22.

Chang, P. Y., Alumbaugh, D. L., Hall, L., and Brainard, J., 2001, Cross well GPR attenuation tomography for identifying clay layers within the vadose zone; Presented at the *2000 American Geophysical Union Annual Fall Meeting*, San Francisco, California.

Hall, L. M., J. R. Brainard, R. S. Bowman, J. H. Hendrickx. 2003. Determination of Solute Distributions in the Vadose Zone Using Down-hole Electromagnetic Induction. *Eos Trans. AGU, 84(46)*, Fall Meet. Suppl., Abstract.

LaBrecque, Douglas j. and Yang, Xianjin, 2001, The Effects of Anisotropy on ERT Images for Vadose Zone Monitoring: VZC-2.

LaBrecque, Douglas J. and Casale, Dan, 2002, Experience with Anisotropic Inversion for Electrical Resistivity Tomography, Proceedings of the Symposium on the Application of Geophysics to Engineering and Environmental Problems (SAGEEP) '02.

LaBrecque, Douglas J., Alumbaugh, David, Brainard, James, and Hall, Laila, 2002, Using ERT with a saline tracer to define vadose zone infiltration, Proceedings of the Symposium on the Application of Geophysics to Engineering and Environmental Problems (SAGEEP) '02.

Liu, S., and T. -C. J. Yeh, Effectiveness of Hydraulic Tomography: Sandbox Experiments, Eos Transactions AGU, 82(47), Fall Meeting Supplement, Abstract H21A-2086, 2001.

Yeh, T.-C. J., 2002,Stochastic Fusion of Information for Imaging the Vadose Zone – in memory of Professor Allan Gutjahr, Eos Transactions AGU, 83(47), Fall Meeting Supplement, Abstract H61E-05 *Invited*.

Zhu, J. and T. -C. J. Yeh, 2002,Stochastic Fusion of Information: An application to Monitoring Water Movement in STVZ Infiltration Field Site., Eos Transactions AGU, 83(47), Fall Meeting Supplement, Abstract H61A-0744.

8.0 Interactions

The tools we developed for the application of ERT to monitoring are being adapted to a number of applications in collaboration with several institutions. Collaborations include work with the Idaho National Engineering and Environmental Laboratory on research in quantifying the movement of water through unsaturated fractured rock and, the application of ERT to monitoring tracer injection in fully saturated environments (Funded by the USEPA and carried out in collaboration with Boise State University), and the application of ERT and EIT (electrical impedance tomography) to the detection of unexploded ordinance in shallow off-shore environments (in collaboration with Zonge Engineering and Research Organization under funding from SERDP). The data analysis strategies have been used during the tests of a prototype autonomous monitoring system tested at the Vadose Zone Research Park at INEEL. This spring, a full-scale version of the system will be installed at a site in South Dakota for monitoring of acid mine drainage.

A short course was held at the University of Arizona in March of 2001 that involved two of the project PI's (Yeh and Alumbaugh). The focus of the course was the use of geophysics for investigating vadose zone hydrology. Also Alumbaugh presented results at the INEEL in February of 2002. Finally, results have been incorporated in an invited paper on vadose zone geophysics to be incorporated into an upcoming book on hydro-geophysics.

9.0 Transitions

ERT methods developed under this project are being applied to the monitoring of mine acid drainage in a collaborative project between USEPA, the Bureau of Reclamation and INEEL. The project will use a fully autonomous ERT system to carry out long term monitoring. Data analysis will be conducted using the difference and anisotropic inversion methods. It is anticipated that this will become the standard method of data analysis for electrical resistivity tomography data collected at vadose zone or mixed saturated/vadose zone remediation sites.

10. Patents

None.

11. Future Work

Work under this research project has emphasized the need to develop a better understanding of the connection between small-scale physical structures and the larger scale geophysical response of these structures. This is the focus of a new EMSP project (Project #86890) which involves fine scale hydrologic

and geophysical forward modeling, coupled with geophysical inversion, to investigate the resolution of geophysical methods for imaging vadose zone flow and transport processes.